

**A Comprehensive Analysis of Polygon Mirror Scanning for
a UAV Based Bathymetric LiDAR**

by

M. S. Greenstein

B.S., University of Colorado, Boulder, 2022

A thesis submitted to the
Faculty of the Graduate School of the
University of Colorado in partial fulfillment
of the requirements for the degree of
Masters of Science
Department of Aerospace Engineering
2024

Committee Members:

Jeffrey Thayer, Chair

Penina Axelrad

Robert Marshall

Greenstein, M. S. (M.Sc., Aerospace Engineering)

A Comprehensive Analysis of Polygon Mirror Scanning for a UAV Based Bathymetric LiDAR

Thesis directed by Prof. Jeffrey Thayer

Light detection and ranging (LiDAR) technology has diverse applications, one notable example being its use in bathymetric mapping. When attempting to use bathymetric LiDAR for small object detection, it is imperative to minimize all possible sources of error to achieve the highest possible resolution. When a LiDAR system employs a scanning mechanism, as systems used for mapping typically do, one of these errors, referred to as a pointing error, comes from uncertainties in the direction in which the scanner is directing the laser beam during data collection. This thesis analyzes the mechanics and behavior of one such LiDAR system through the lens of previously defined assumptions about its behavior. The goal was to empirically and theoretically determine the pointing accuracy of this bathymetric LiDAR system. The desired specification for ground resolution accuracy for this system is 5cm. At a nominal flight altitude of 30m, this requires a pointing accuracy of less than 0.1° . The system underwent multiple tests and processing algorithms to optimize its pointing capabilities. Results showed improvements in relative alignment of the data throughout capture, expected scanned object sizes, as well as an increased general understanding of the system's pointing behavior. This paper also suggests possible mechanical solutions to enhance the system's pointing capabilities further.

Dedication

To my parents who have instilled in me an appreciation of education and strong sense of self. Who through all my fears and stress never doubted me once. I love you both so much, I would not be here without you.

To my cherished friends, whose support and patience was not taken for granted.

And to all the girls on their journeys in STEM in classrooms full of boys. Wreck them, ladies.

Acknowledgements

I'm incredibly grateful to my advisor, Jeffrey Thayer, for his guidance and support over the past two years. He took me on as an undergraduate senior just trying to break into the field of remote sensing and provided me with more resources and guidance than I ever could have hoped for.

I would also like to express my deepest appreciation to Kevin Saccia for mentoring me and generally being a great resource. His trust and confidence in me meant the world, and I could not have done this without him.

Thank you to LiteWave for granting me access to their LiDAR system and its data and permission to present it for this research.

Thank you to Penina Axelrad and Robert Marshall for being on my defense committee and providing me with invaluable feedback to complete this paper.

This material is based upon work supported by the US Army Corps of Engineers and the Department of Defense Strategic Environmental Restoration Development Program under Contract No. W912HQ22C0042. This research was supported in part by the U.S. Department of Defense, through the Strategic Environmental Research and Development Program (SERDP). Views, opinions, and/or findings contained in this thesis are those of the authors and should not be construed as an official department of defense position or decision.

Contents

Chapter

1	Introduction	1
2	LiDAR Scanners	12
3	Data Processing Methods and Analysis for a Polygon Mirror LiDAR	18
3.1	Initial Assumptions for Data Processing	18
3.2	Modeling Polygon Mirror Scanning Behavior	22
3.3	Computational Pointing Improvements	29
3.3.1	Defining an Algorithm	29
3.3.2	Measurement Tests	32
3.3.3	Boresighting	41
3.3.4	Calibration	43
3.3.5	Averaging and Error Analysis	47
4	Conclusions	55
4.1	Assumption A1	55
4.2	Assumption A2	56
4.3	Assumption A3	57
4.4	Overall Conclusions	57
5	Further Work	59

Bibliography	62
---------------------	-----------

Figures

Figure

1.1 Fully processed coastal bathymetric point cloud colored by relative altitude of ground points.	2
1.2 Fully processed coastal bathymetric point cloud taken in a similar area as Figure 1.1 and colored in the same manner.	3
1.3 Color scale used for Figures 1.1 and 1.2, and all subsequent point clouds. Blue is the lowest relative surface altitude and red is the highest.	3
1.4 Photograph of the beach captured in the point clouds.	4
1.5 Top-down view of the point clouds overlayed on an image of the beach they were taken on.	5
1.6 Graphical description of Snell's Law and Fermat's Principle described by a subaqueous isosceles triangle.	8
1.7 Point placement effects of an incorrect pointing angle. The x and z axes represent the LiDAR body scan plane.	9
1.8 Fermat's Principle for water with a wavy surface. The green point represents the return with no refraction correction, the red point is a correction assuming a flat surface, and the yellow point is the true correction with the wavy surface. The incident angle on the flat surface is -10.0° while on the wavy surface, with reference to the dotted normal, the incident angle is 12.2°.	11
2.1 Example of a real polygon mirror[23].	13

2.2	Example of a real single galvanometer scanning mirror[18]	14
2.3	Outline of the important parameters for a polygon mirror[5].	15
2.4	Figure describing the motion and angles during a polygon mirror scan.	16
3.1	Illustration of laser path within Maverick from where it hits the polygon mirror to where it exits the output aperture.	19
3.2	Example of an expected output from all three detectors in Maverick. With a laser pulse rate of approximately 20kHz, the D3 output pulse detections look continuous compared to D1 or D2.	21
3.3	Simulated geometry of the light reflection from a polygon mirror using the parameters of model A. The beam at -30° hits the mirror at $x=4.11\text{cm}$, at 0° hits at $x=3.93\text{cm}$, and at 30° at $x=4.37\text{cm}$	23
3.4	Simulated geometry of the light reflection from a polygon mirror using the parameters of model B. The beam at -30° hits the mirror at $x=2.73\text{cm}$, at 0° hits at $x=2.83\text{cm}$, and at 30° at $x=3.27\text{cm}$	23
3.5	Required measurements within Maverick to create an accurate simulation.	24
3.6	Adding an aperture to the simulation with the parameters of model A: $a = 4.5\text{cm}$ and $z_{laser} = -3.75\text{cm}$	26
3.7	Adding an aperture to the simulation with the parameters of model B: $a = 4\text{cm}$ and $z_{laser} = -4\text{cm}$	26
3.8	Model of significant output angles derived from Maverick system specifics, with the D1 detector added as the blue square.	28
3.9	Modeling the expected detection assuming a symmetric cone vs actual point placement given the known offsets.	29
3.10	Experimental point cloud that has been processed using poor assumptions as described above.	31
3.11	Gaussian distribution of elevation values for the cloud displayed in Figure 3.10.	31

3.12 All measured distances in the wall measurement test. Points a and f are each extreme end of the scan, where negative angles are on the side of a and positive on the side of f. Points b and d are where the scan was cut off by each end of the aperture. Point e is where the scan was cut off by the D1 detector, and point c is the direct horizontal point to the center of the aperture. Line g indicates the distance from that point c and the center of the aperture.	33
3.13 Zoomed in view showing the angles exiting the aperture and the offset angle in the wall test.	34
3.14 Reprocessing of the same point cloud shown in Figure 3.10 using the angles from the wall test.	36
3.15 Gaussian distribution of elevation values for the cloud displayed in Figure 3.14. . . .	36
3.16 Collection of detections made by Maverick and their recorded travel times from output to reception.	39
3.17 Adding where the 0° angle was placed within a swath as compared to where it should be - at the smallest travel times.	39
3.18 Next point cloud reprocessing using the offset from the least-time test.	40
3.19 Gaussian distribution of elevation values for the cloud displayed in Figure 3.18. . . .	41
3.20 Boresighting Demonstration	42
3.21 Same cluster of points shown in Figure 3.20 when the point cloud is fully boresighted. .	43
3.22 Stretching or compression effects of having an incorrect D1 angle.	44
3.23 Dimensions of a real cross calibration target that is scanned by Maverick.	45
3.24 CCT apparent dimensions using different D1 angles.	45
3.25 Reprocessing the point cloud using the updated optimized D1 angle.	46
3.26 Gaussian distribution of elevation values for the cloud with an optimized D1 angle displayed in Figure 3.25.	46
3.27 Takeoff Area	47

3.28 Physical description of the time ratio that should be consistent throughout data collection. t1 is the time between D2 and D1 and t2 is the time from D1 back to D2.	48
3.29 Different types of reflection [10].	49
3.30 Reprocessed point cloud but with the addition of averaging to find the central swath points.	50
3.31 Gaussian distribution of elevation values for the cloud with averaging added displayed in Figure 3.30.	51
3.32 Final fully boresighted point cloud.	53
3.33 Gaussian distribution of elevation values for the final cloud with all corrections applied displayed in Figure 3.32.	53
3.34 Final fully boresighted point cloud overlayed onto the beach.	54
5.1 Simulated changes resulting in a 0° central angle.	61

Chapter 1

Introduction

There are many difficulties to navigate in order to map and analyze shallow coastal regions effectively. The limited depth of the water makes the typical underwater mapping tool, sonar, challenging to use due to its large size and requirement to be touching the water surface for operation [19]. Other terrestrial mapping tools, such as radar or other electromagnetic (EM) wave transmitters, cannot penetrate the water surface. A relatively new technique called Airborne LiDAR Bathymetry (ALB) has emerged as a promising solution for mapping the ocean floor in shallow water regions [6] [14]. ALB is a form of active remote sensing that emits and tracks EM waves within the visible light band to map these underwater surfaces, also known as the bathymetry. ALB allows operation from above the water's surface, making shallow waters more accessible for thorough analysis.

All current ALB systems share some common characteristics, most notably their operating wavelength of 532nm, as it is a well-developed wavelength of laser technology [7] and falls within the green band of the EM spectrum, allowing for high transmission levels through water. ALB systems can be flown on any airborne platform, commonly airplanes or unmanned aerial vehicles (UAVs), but the system for this study exclusively operates on a UAV. Typical applications of this technology include general survey of an area of interest, environmental studies such as coral reef mapping[2] or coastline tracking[11], and water volume calculations[16].

Most ALBs fall into the category of ranging LiDARs, characterized by an ability to very precisely time-tag laser pulse travel times. LiDAR systems time these pulses to sub-nanosecond

resolution for high-fidelity data. ALBs also consistently possess scanning abilities to capture swaths of points as the vehicle moves in space. Section 2 discusses different ways to design the scanning subsystem. Reliable pointing control is necessary to drive the beam along the area of interest, but it may lack precision due to scanning mechanism limitations. Reliable pointing knowledge for every output laser shot is ultimately more important for high point precision.

The ultimate goal of ALB mapping is to produce a point cloud - a high-density collection of points that, if everything within the system behaves correctly, should reveal a high-quality replica of the surveyed area. Two examples of this, and the product of the work in this thesis, are shown in Figures 1.1 and 1.2. In both point clouds, the green layer above a blue layer is the water surface sitting above the bathymetry. In the survey shown in Figure 1.1, the bathymetry reaches approximately 7m in depth, and the second survey shown in Figure 1.2 only reaches approximately 2m. The coloring in both of these images and all point clouds presented throughout this thesis is based on the relative surface altitude, graded by the color scale defined in Figure 1.3.

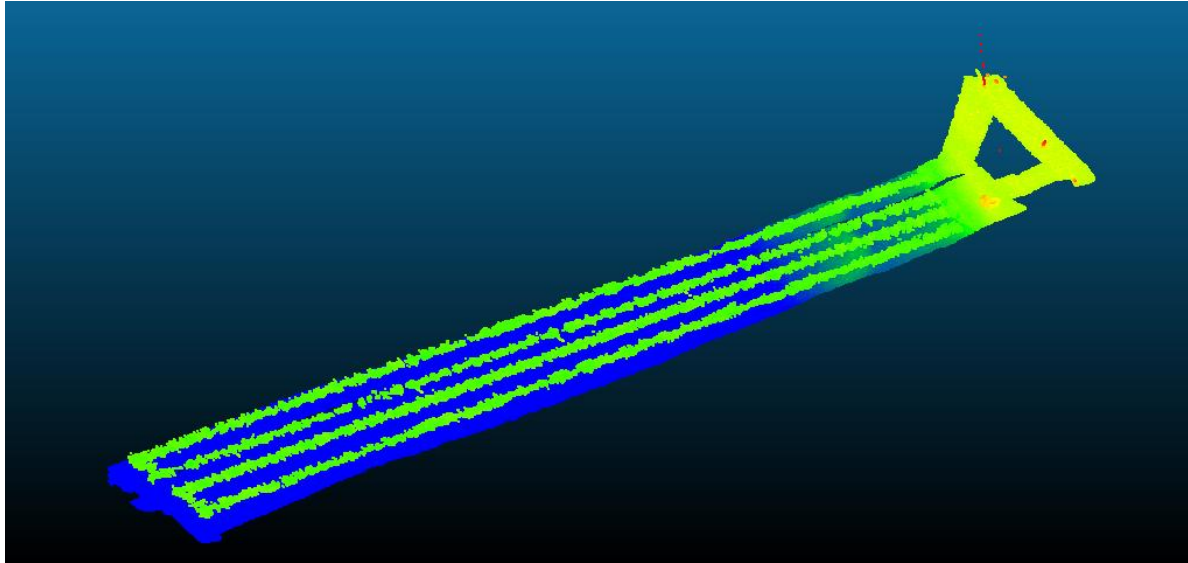


Figure 1.1: Fully processed coastal bathymetric point cloud colored by relative altitude of ground points.

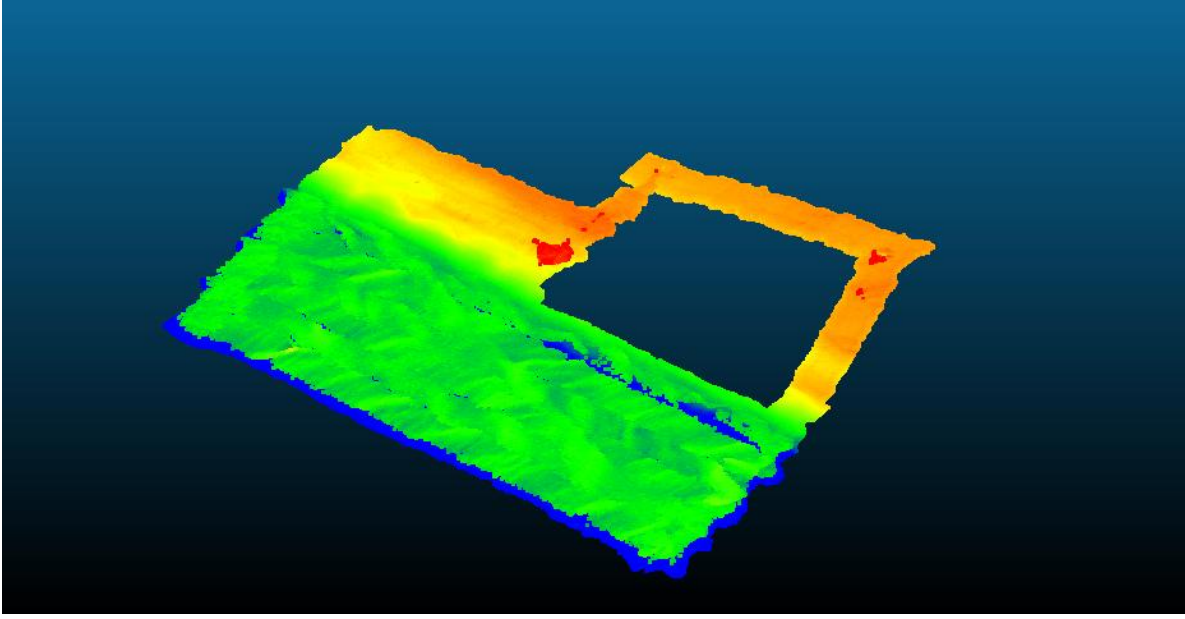


Figure 1.2: Fully processed coastal bathymetric point cloud taken in a similar area as Figure 1.1 and colored in the same manner.

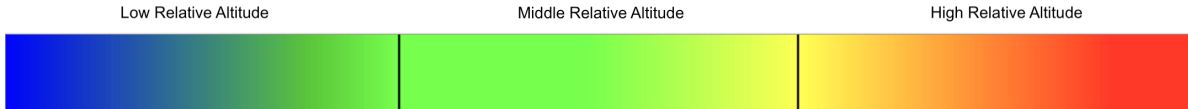


Figure 1.3: Color scale used for Figures 1.1 and 1.2, and all subsequent point clouds. Blue is the lowest relative surface altitude and red is the highest.

Both point clouds come from a campaign performed using the LiDAR system that is the subject of interest in the coming chapters. It can be difficult to discern what the area of interest actually looks like by the point clouds alone. Therefore, the image in Figure 1.4 shows a side view of the beach area mapped by the cloud. For even more orientation, Figure 1.5 shows these point clouds overlaid onto a bird's eye view of the area. This figure also shows how the two clouds overlap.



Figure 1.4: Photograph of the beach captured in the point clouds.

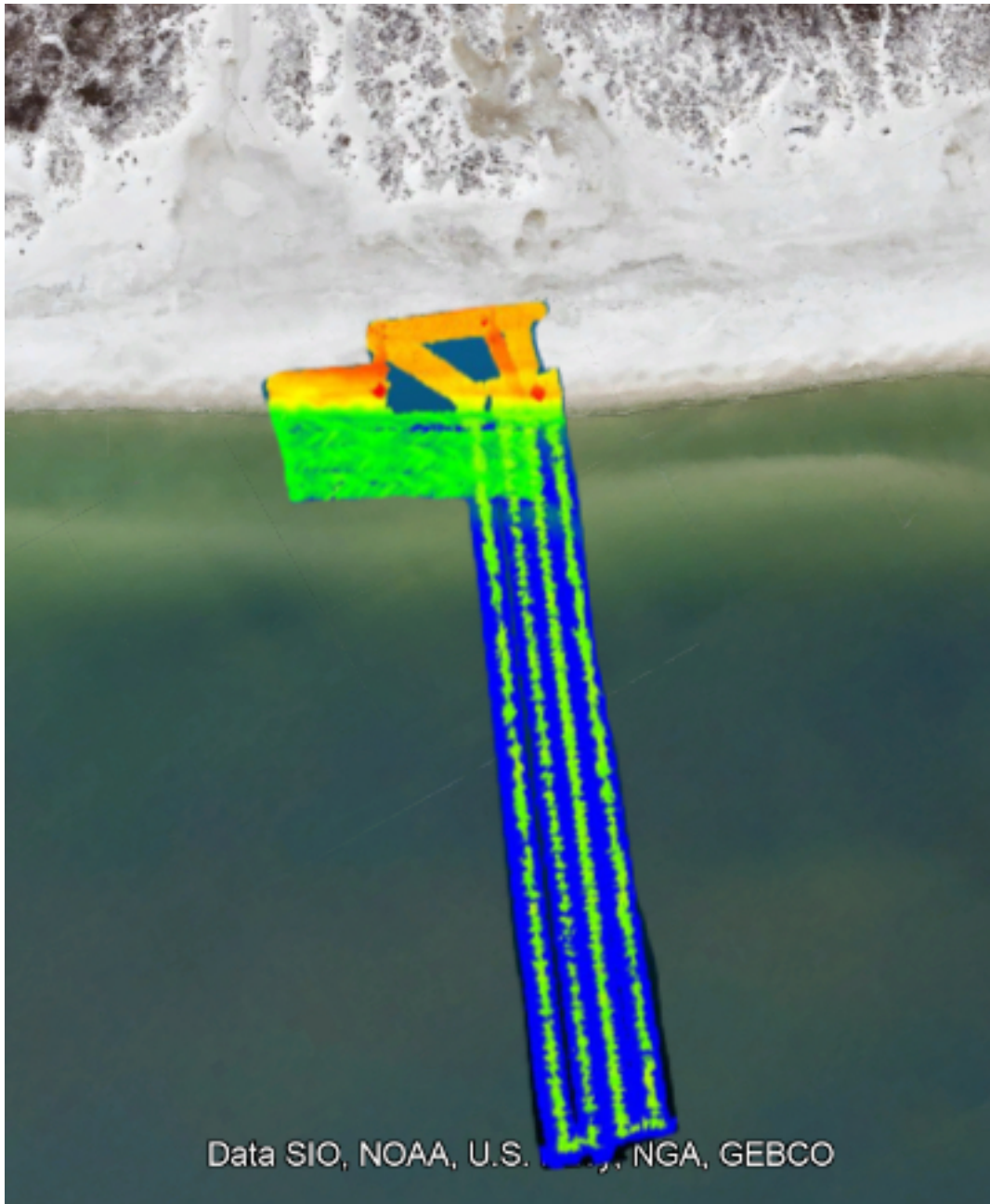


Figure 1.5: Top-down view of the point clouds overlaid on an image of the beach they were taken on.

At its core, a scanning and ranging LiDAR requires three pieces of information: a reference position, a time, and an angle. The system uses a Global Positioning System (GPS) sensor and an inertial measurement unit (IMU) to calculate the reference position. It is important to have precise

position and orientation information from these sensors so each detection point has a well-defined origin. The time measurement encapsulates the main principle of LiDAR, describing the time it takes for a beam of light to exit a system, scatter off an object back toward the source, and be detected again – often referred to as a time-of-flight measurement. The system calculates a range between the UAV and the scatterer using the speed of light and the index of refraction (IOR) of the propagation medium. When the LiDAR is scanning, it is also imperative to know the position of the scanning component when the pulse leaves the system to resolve the pointing angle of the output pulse and properly place the detection in a global reference frame.

The uncertainty in a UAV position comes directly from the GPS/IMU unit the system uses. These errors can be minimized using real-time or post-processing techniques. Both correction techniques involve a base station - a stationary receiver that will compare the reported GPS solution of a moving object. A suitable technique for applications like ALB that do not require real-time solutions is post-processed kinematics (PPK), which uses the base station data in conjunction with updated GPS satellite records to produce a final UAV position solution. For this project, an SBG Systems Unit[22] and base station collected all GPS and IMU data, and the SBG processing software, Qinertia, performed all the necessary corrections.

On the other hand, uncertainties related to timing and pointing angle are all ALB system-based and can be made larger or smaller with different combinations of physical components or processing techniques. All uncertainties related to these two measurements fall into subcategories of timing, ranging, or placement issues. The subcategory of any particular uncertainty is decided by whether it affects the point placement before (timing), during (ranging), or after (positioning) a detection is assigned a distance from the system. These distinctions are important for understanding how to quantify and minimize all uncertainties.

Beginning with timing, the most straightforward source of uncertainty is the actual timing resolution of the detectors. Every pulse received is time-tagged and put into a bin of a minimum time resolution size and simply cannot be resolved further. Every output laser pulse has a finite output shape and size. As this pulse travels, it scatters off different surfaces and volumes, convolving the

pulse with the scatterer causing its initial shape to distort. Uncertainties in the return pulse shape can cause variability of where within the detected pulse the scattering event occurred. Coupled with this issue is the actual probability distribution of photons on the detector. An advanced statistical model can be used to determine where the scattering happened within the stream of photons and pulse shape, however, there is inherent uncertainty in the accuracy of this process.

For any LiDAR system, the pulse shape timing uncertainty also translates to a ranging uncertainty of $\Delta r = \frac{v\tau}{2}$, where τ is the pulse width in seconds. This invokes another ranging-domain uncertainty, the propagation medium's IOR. The IOR for air is assumed to be the same as a vacuum, $n_{air} = 1$, and for water, $n_{water} = 1.33$. These values directly describe the speed at which light travels through that medium. The equation $v = c/n$ (c is the speed of light, 299 792 458 m/s) defines the exact velocity. Both values are good standard assumptions, especially for air, however, the water IOR is slightly affected by the water column's salinity and temperature. The IOR is a big issue for ALB systems because the LiDAR system cannot resolve when the beam passes from air to water. The system instead assumes the transmitted beam was traveling in the air the whole time and places the point accordingly at a greater distance than its actual position. This assumption is an issue in range, as the distance traveled in water rather than air in the same amount of time is 33% less due to the larger IOR. Processing techniques are used to correct this range as precisely as possible, as will be discussed in Chapter 3. This uncertainty also causes an angular displacement because the entrance of the beam into the water experiences an angle of refraction, as described by Snell's law.

Snell's law, shown in Eq 1.1, states that when a beam of light travels between two media, the light bends depending on the ratio between their IORs. In Eq 1.1, the n_1 and θ_i represent the IOR and incident angle of a beam of light on one side of the barrier between mediums 1 and 2. n_2 and θ_r are the index of the second medium, and the refraction angle on the other side of the barrier. It is also important to appreciate the underlying physics of Fermat's Principle to comprehend Snell's law. Fermat's Principle states that "light travels between two points along the path that requires the least time, as compared to other nearby paths" [1]. Snell's law then provides the physical

description of the angles that describe this path of least time. The result of this equation is an equilateral triangle defined by the angles α and γ , and the path length a as shown in Figure 1.6. B' here is the point placement assuming no change of index. The actual length a is related to the measured length OB' as $a = \frac{n_{air}}{n_{water}} OB'$. The angle θ_i here is equivalent to the output pointing angle, so using the known IORs of air and water, θ_r is solved for. α is calculated as the difference between these incident and refraction angles, which is then used to find the real location of return, point C.

$$n_1 \sin(\theta_i) = n_2 \sin(\theta_r) \quad (1.1)$$

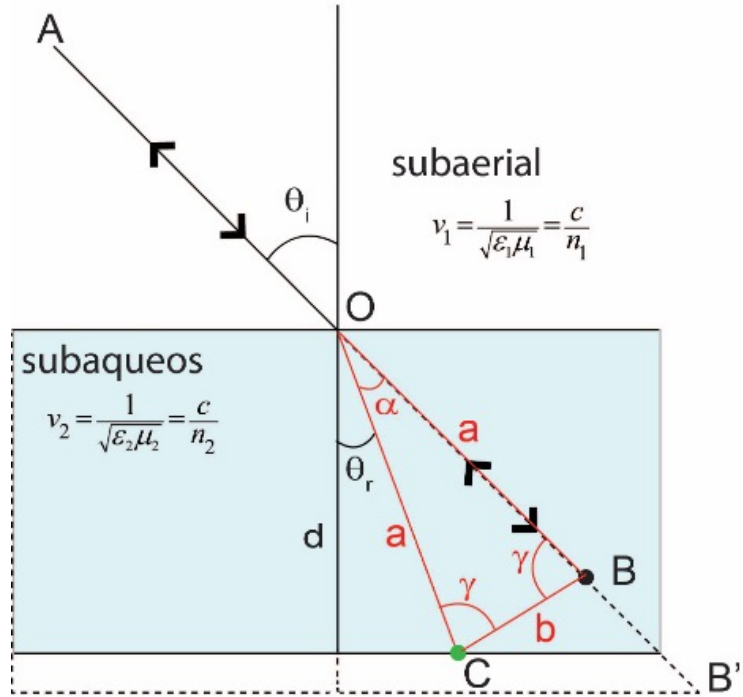


Figure 1.6: Graphical description of Snell's Law and Fermat's Principle described by a subaqueous isosceles triangle.

This thesis focuses on uncertainty in the LiDAR beam pointing angle, which is within the placement uncertainty domain. Every detection is assigned an angle within the scan plane of the

LiDAR body frame based on the assumed instantaneous position of the scanning component at the exact moment of pulse transmission. The system places the point at a distance r based on the time, from the instantaneous origin O determined by the GPS/IMU sensor, at this angle θ relative to the normal axis, also defined by the IMU. This angle also defines the beam's incident angle on the water, θ_i . If a detection with a range r transmits at an angle θ in the scan plane but is incorrectly assigned a pointing angle, θ_{err} , there will be errors in both the x and z position of the detection. An illustration of this can be seen in Figure 1.7 where θ_{err1} and θ_{err2} are two possible incorrect angles of a return with range r .

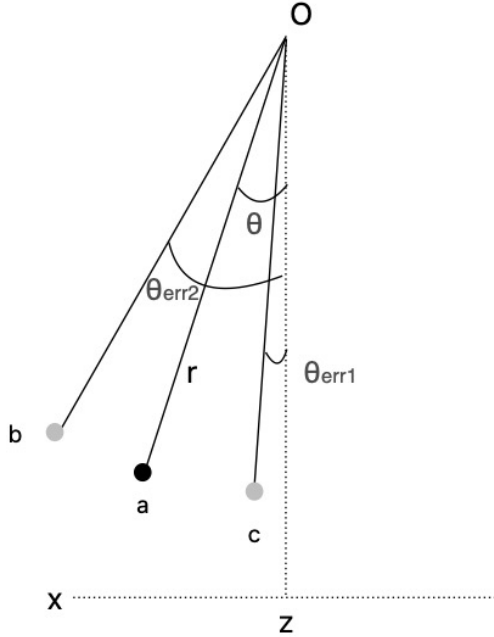


Figure 1.7: Point placement effects of an incorrect pointing angle. The x and z axes represent the LiDAR body scan plane.

When discussing uncertainties in ALB data, it is vital to acknowledge the presence of surface waves and their impact on the direction of the light. All discussion thus far, and all that continue

through this thesis, assume that the water is a perfectly flat surface. Generally, calm waters are necessary to receive robust ALB data, supporting the validity of this assumption. However, any slope in the water surface changes the incident angle and, subsequently, the refraction angle of the beam of light, modifying the path that the light travels in the water. The incident angle is defined by the slope of the water surface and its normal at the point of light penetration. For flat water, that normal aligns directly along the z-axis and means the incidence angle is equal to the pointing angle. A wave will rotate it, as shown in Figure 1.8. This behavior is impossible to understand without initial uncertainty quantification and mitigation of the pointing angle. Particularly, without pointing uncertainties quantified, it is impossible to decouple pointing angle errors from wavy surface errors. Therefore, this thesis focuses on providing a comprehensive review of ALB scanning and analysis of pointing angle retrieval and accuracy.

The upcoming chapters will begin with an exploration of different types of scanning mechanisms, followed by a description of the work completed for this thesis. The culmination of that work is then discussed in the conclusion section, and then the thesis closes with recommendations for further work.

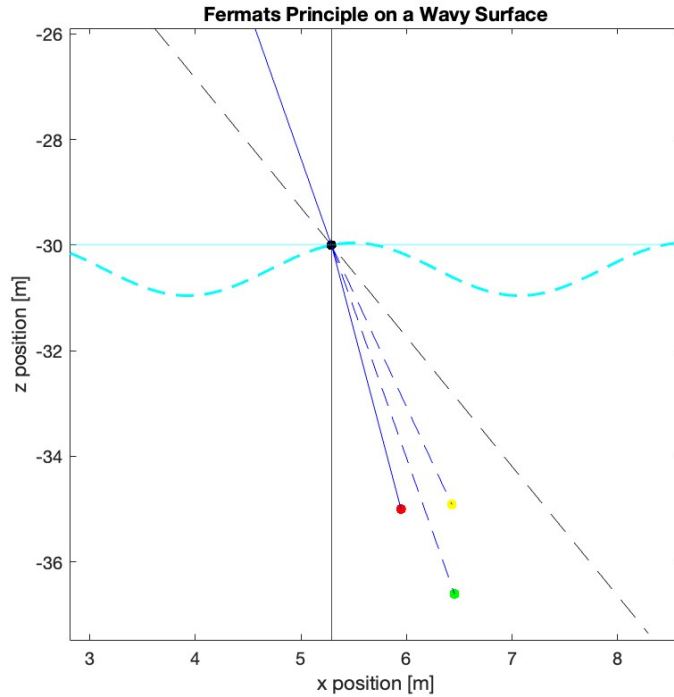


Figure 1.8: Fermat's Principle for water with a wavy surface. The green point represents the return with no refraction correction, the red point is a correction assuming a flat surface, and the yellow point is the true correction with the wavy surface. The incident angle on the flat surface is -10.0° while on the wavy surface, with reference to the dotted normal, the incident angle is 12.2° .

Chapter 2

LiDAR Scanners

Before characterizing the uncertainty in a pointing angle, it is essential to comprehend how the system generates this angle. Various LiDAR applications and system types employ diverse scanning mechanisms, categorized based on both their physical attributes and output dimensionality. Some LiDAR applications, such as atmospheric measurement, do not require scanning. In these 1D cases, the initial pointing direction remains constant throughout data collection unless there is bulk unit movement. However, to achieve comprehensive area visualization in mapping LiDARs, 2D or 3D scanning is imperative. For LiDAR systems utilized in navigating self-driving cars, 3D scanning is essential to ensure a complete understanding of the overall environment and the presence of objects and people surrounding the vehicle. Conversely, UAV-based mapping LiDARs can suffice with a 2D scanning system, as the third dimension comes from the movement of the UAV.

Within this 2D scanning requirement, there are many scanning mechanisms to choose from. The most common methods fall into two categories: opto-mechanical scanning and micro-electro mechanical scanning (MEMS). MEMS scanners are an extremely small and lightweight option compared to opto-mechanical scanners. Their driving principle is to use electromagnetism to steer the beam rather than a much larger component, such as an electric motor. MEMS are typically used in smaller, more controlled situations such as endoscopic scanning for cancer identification [24]. While there is promise for using MEMS scanners within UAVs, in their current state of development, the technology needs to be more robust to operate in that airborne environment. Specifically, they are limited by a small FOV, low scan rate, and insufficient control stability[21].

There is another noteworthy type of 2D scanning called solid-state scanning. This method is different because there is not a moving mechanism; rather, a unidirectional beam is split into beamlets so all data is taken simultaneously instead of using a sweep through all scan angles. This approach would theoretically be ideal for a UAV-based LiDAR, as it would remove the need to track instantaneous pointing angles and could also achieve extremely high point density [21]. However, applying solid-state scanning is too expensive and requires too much power to be feasible for scientific or commercial ALB work.

The most straightforward 2D scanning type is opto-mechanical scanning, which uses mechanically steered optical components such as mirrors or prisms to direct the light in the desired direction at any given moment. Two standard optical components used for this purpose are polygon mirrors (PMs) and single galvanometer scanning mirrors (GSs). Both systems have a static beam that reflects off a moving mirror driven by some electrical motor. GSs steer using a single flat mirror that moves back and forth in an oscillating motion. The beam reaches its extreme pointing angles right at the edge of each oscillation. At this point, the mirror stops and then begins to move in the opposite direction, meaning its velocity must start and resume in the opposite direction. PMs steer using a polygon-shaped mirror that rotates about its central axis. Each edge of this polygon is a facet. PMs theoretically have a constant rotational velocity because the beam reflects off the next facet in the rotation at the end of one scan instead of the mirror needing to change its velocity. Figures 2.1 and 2.2 show real examples of a PM and a GS, respectively.

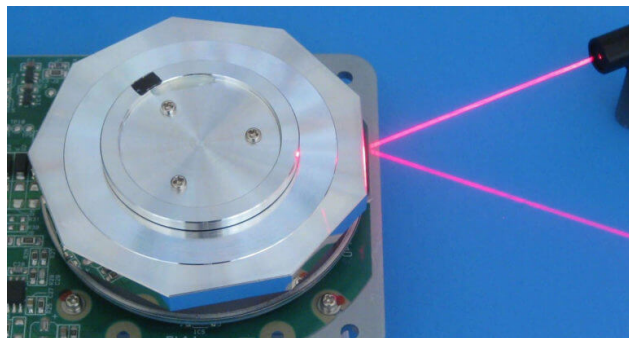


Figure 2.1: Example of a real polygon mirror[23].



Figure 2.2: Example of a real single galvanometer scanning mirror[18].

In earlier stages of scanning LiDAR in the 1990s, the primary scanning system was GSs because of their large field of view (FOV) capacity and generally high scanning resolution. However, in the 2000s, PMs gained popularity because of their high scanning velocity [5]. Another critical difference between these options is the coupling between the scan frequency, f_{scan} , and the FOV. There is an exponential decrease in the controllable FOV with a higher f_{scan} in GSs, whereas there is no coupling between these two parameters for PMS. GSs are also a much simpler design, characterized by the size of the aperture, mirror pivot point, and distance from the aperture, whereas PMs require three more parameters for characterization. These parameters include the polygon's apothem, the laser beam's eccentricity from the mirror pivot point, and the number of facets. While this additional complexity requires extra analysis, it also allows for more control over the scan behavior[5].

With all the above considerations, this thesis focuses on a LiDAR system that uses a PM. The general high resolution of PMs and their high velocity and large FOV abilities are desirable characteristics for UAV-based LiDAR applications. Additionally, there are demonstrations of their robustness for this specific application [21] [5].

Before discussing how they work within a LiDAR system, general PM behavior and component analyses are necessary. Figure 2.3 comes from one specific study on the behavior of PMs and

GSs for laser scanning and does a nice job illustrating the different important parameters. Any regular polygon only needs one geometric parameter to define the face shape fully. Regardless, this diagram outlines both the apothem, R , and the side length, a . The height, b , is illustrated, but in the context of laser scanning, this is less important as long as it is large enough to capture the full beam spot. What is somewhat misleading about this drawing is the apparent cone of light it shows exiting from a single point. With some initial analysis, it became evident that this is not an accurate model for the behavior of the light reflecting off the mirror.

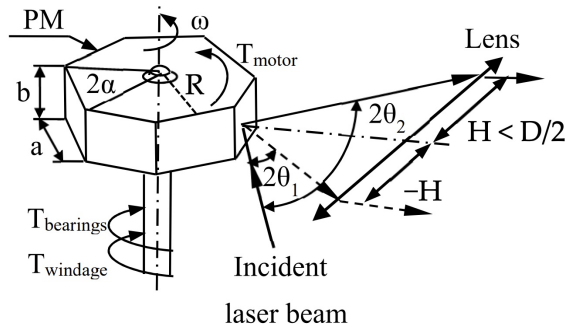


Figure 2.3: Outline of the important parameters for a polygon mirror[5].

Figure 2.4 shows a different view of this process, highlighting the inconsistencies in this cone shape and the general lack of a central axis. There are a few things to note about this figure before discussing the reasons for this. First, the output angle of the beam is directly related to the angle of mirror rotation with $\theta_{beam} = 2\theta_{mirror}$. Consequently, when the beam is reflected directly downward in the $-z$ direction at a 90° angle, the mirror only performs a 45° rotation. The PM used for this representation is octagonal, so the number of facets, n , is 8. A core property of all PMs is that the number of facets the PM has fully defines the angular range of the scan. In Eq 2.1, α is the angle the mirror must travel for a beam to go from one side to the other of a mirror facet. When $n=8$, $\alpha = 45^\circ$ and the pointing range is double that, or 2α , meaning an 8-facet PM has a pointing span of 90° .

$$\alpha = \frac{2n}{\pi} \quad (2.1)$$

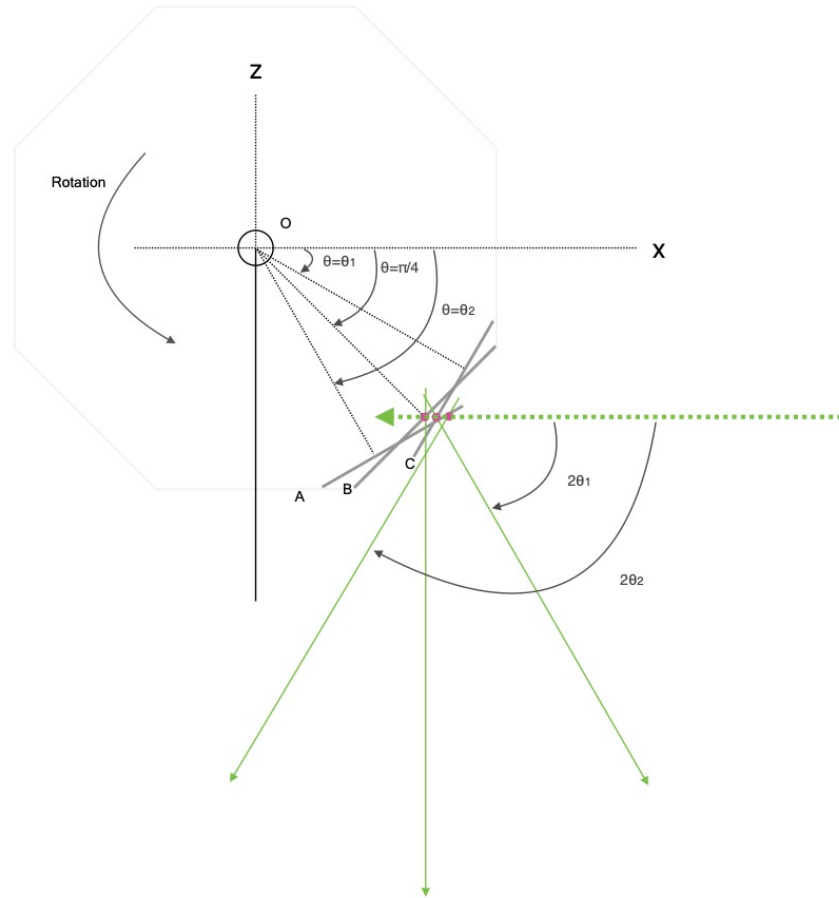


Figure 2.4: Figure describing the motion and angles during a polygon mirror scan.

In reality, there is no central axis of the reflected beams. The $2\theta_1$ and $2\theta_2$ beams occur further to the right on the x-axis than the directly downwards beam. While this specific layout is due to the sizes of components and geometry used for the drawing, the general concept that these are not all reflected from the same point on the x-axis is a significant property of PMs. A, B, and C in Figure 2.4 represent three different facet positions that result in the illustrated pointing

angles. The way these facet positions propagate through time as the PM spins around the origin O is what leads to this x translation. With this initial understanding of PM properties, a specific LiDAR system that uses a PM is analyzed in Chapter 3.

Chapter 3

Data Processing Methods and Analysis for a Polygon Mirror LiDAR

The following sections explore one example of a prototype polygon mirror scanning LiDAR system developed by LiteWave Technologies, Inc. LiteWave has granted access to this prototype LiDAR system and approved a general discussion and analysis of its design. The exact metrics and dimensions of this system are considered proprietary. This prototype system is referred to as Maverick for the remainder of this thesis.

For Maverick to attain the desired level of small object detection, it must achieve 5cm of horizontal accuracy in point placement. For a UAV flying at 30m above 5m deep water with a flat surface, the pointing uncertainty to achieve this level of accuracy must be less than $\pm 0.1^\circ$. This is the driving requirement for all the work presented in this chapter.

3.1 Initial Assumptions for Data Processing

Polygon mirrors alone are an effective way to direct a laser through a swath of angles; however, for a fully functional LiDAR system, there must be additional elements to detect and record the mirror position during rotation. The information from these additional elements defines the pointing angle of the beam within the scan plane. One way to almost perfectly track this would be to have an array of detectors surrounding this mirror, recording the angle exactly at every output laser pulse. However, this is unrealistic, given power, space, and monetary requirements. Therefore, a creative solution must be introduced to minimize the cost within all these requirements while still providing enough information to meet the pointing angle uncertainty requirements.

Maverick uses only one detector at a point within the scan plane to extrapolate all pointing angles within a swath. The difference between a swath and a scan is that a scan is the period that the laser reflects off of one facet from beginning to end, while a swath is just the portion that actually exits the output aperture. Maverick uses an octagonal mirror to create these scans, just like the mirror shown in Figure 2.4. A diagram of this system, showing the path from the internal laser to the system aperture, is shown in Figure 3.1. Note that in this figure, as well as all non-point cloud figures shown, the component sizes and distances are not to scale.

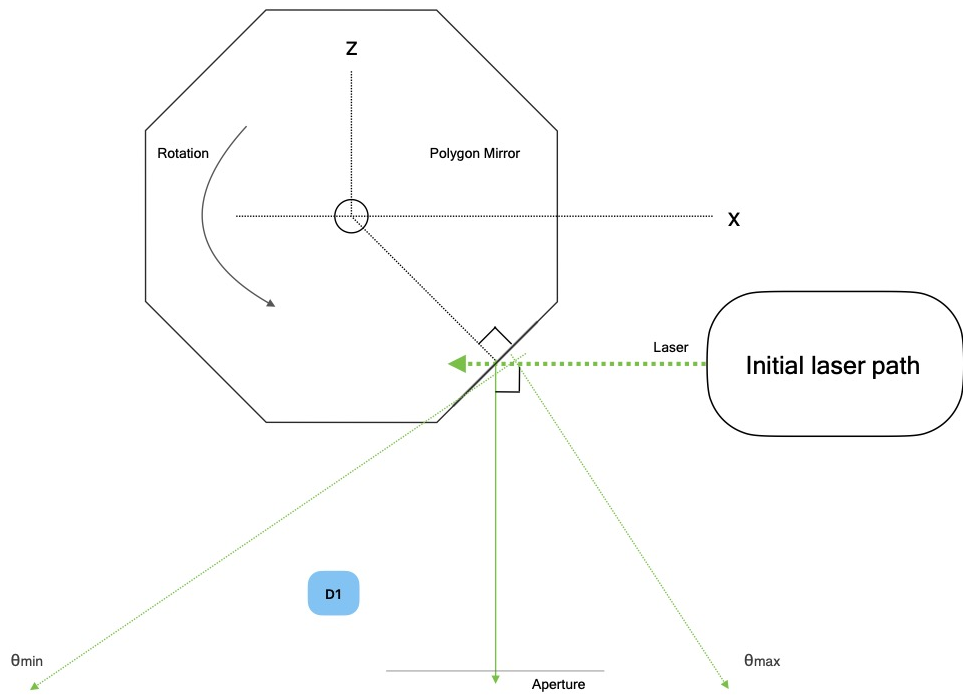


Figure 3.1: Illustration of laser path within Maverick from where it hits the polygon mirror to where it exits the output aperture.

The three output pieces of data that determine the point cloud relative to the unit information are the once per-swath mirror detector (D1), the LiDAR receiver (D2), and the output pulse detector (D3) that records every laser pulse before it exits the system. The D2 and D3 detectors are not

shown in Figure 3.1, as the D3 detector exists as part of the initial laser path section, and the D2 detector is on a slightly different plane within the LiDAR system. Physically, the laser begins by outputting a pulse of light. Most of that light travels through the system, but a small portion is directed to the output pulse detector, D3, to record the time of that pulse. It eventually reaches the PM and, as shown in Figure 3.1, when the PM is at a certain angle, the beam hits the D1 detector. Due to the counter-clockwise rotation of the mirror, it is after this intersection with D1 that the beam exits the aperture, allowing the laser light to scatter off of objects outside of the system and be received by the LiDAR D2 detector. Figure 3.2 shows a mock schematic of these detections. One thing of note is that the entire scan does not exit the aperture and thus is not included in every swath, as illustrated in both Figure 3.1 and 3.2. This behavior is why, in Figure 3.2, there are sections where the output D3 pulses are still detected, but nothing is received. In the current design of Maverick, only about 1/3 of the scan actually provides returns. Besides a general waste of power, this can also create excess noise within the system, increasing the processing difficulties. Section 5 discusses possible solutions to increase the number of output pulses per scan.

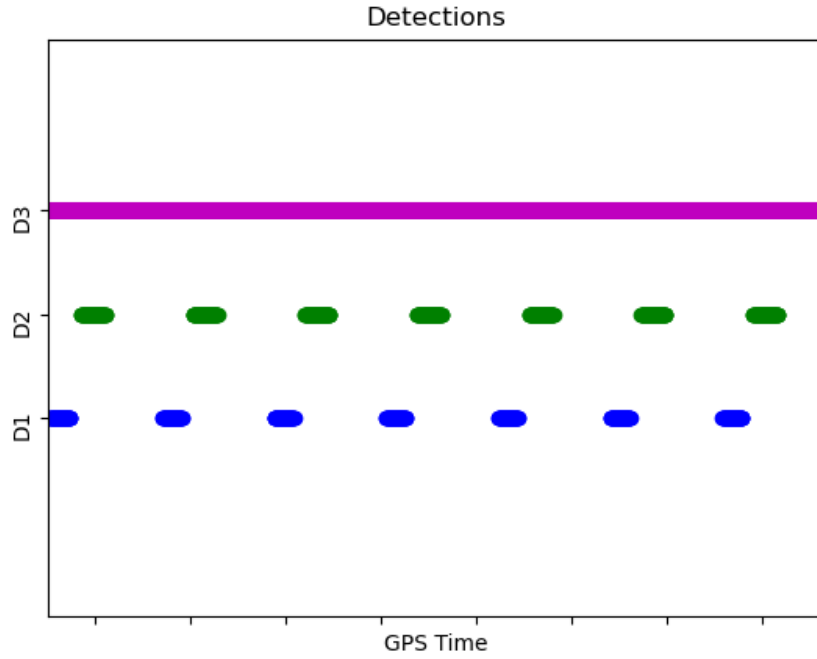


Figure 3.2: Example of an expected output from all three detectors in Maverick. With a laser pulse rate of approximately 20kHz, the D3 output pulse detections look continuous compared to D1 or D2.

The knowledge of the D2 and D3 times is enough to assign a range to every point. Specifically, each D2 detection time is assigned to the D3 detection time that occurred right before, and the time difference between those, multiplied by the speed of light, determines the apparent range. Then, combining the information of D1 and D2 detection times provides the basis for the pointing angle determination of each return. The remainder of this section discusses different methods explored to quantify this information. These methods begin with three main underlying assumptions - every scan contains evenly distributed pointing angles (A1), the pointing angle in the middle of the aperture is 0° (A2), and a swath spanning 30° exits the aperture (A3). Prior to this research, Maverick point cloud production relied on all these assumptions. This research attempts to improve pointing knowledge by investigating their validity.

3.2 Modeling Polygon Mirror Scanning Behavior

The first step in analyzing these assumptions was creating a generic 2D PM model. The main goal of this model was to learn what angles actually exit the aperture compared to the assumptions, and quantify the asymmetric effects discussed in Section 2. To begin, the MATLAB function 'nsidepoly' was used to create an 8-sided PM with a side length a about an origin o , with a defined rotation angle ϕ from the normal. Because it is a regular polygon, just the side length fully defines all dimensions of this polygon. Next, a laser path is defined to hit the mirror using a laser origin and direction of travel. No laser losses are considered in this model, so the x position of this origin is inconsequential. However, the z position is quite important as it changes where on the facet the laser must hit to produce certain angles and thus adjusts the path of those angles relative to the fixed exit aperture. To capture the properties of a real mirror, at the point where the laser hits the mirror, the reflection angle θ_r is set equal to the incident angle θ_i .

Figure 3.3 shows an example, A, of this model that uses the same parameters as those for the drawing in Figure 2.4. In this example, $a = 4.5\text{cm}$ and $z_{laser} = -3.75\text{cm}$, where the $(0,0)$ is the mirror's center. This results in both of the outer angles, -30° and 30° , intercepting the mirror at higher values on the x-axis than the vertical 0° angle. Adjusting the parameters within this model showed that the most symmetric angle distributions came when the side length and the z laser position were similar magnitudes. Figure 3.4 shows an example, B, with the mirror parameters adjusted so that $a = 4\text{cm}$ and $z_{laser} = -4\text{cm}$. While still not symmetric, this model at least has the origin of the 0° angle in the center of the two larger outer angles.

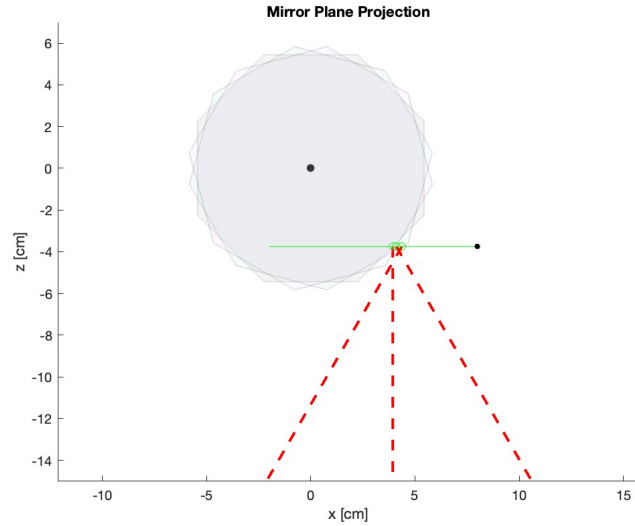


Figure 3.3: Simulated geometry of the light reflection from a polygon mirror using the parameters of model A. The beam at -30° hits the mirror at $x=4.11\text{cm}$, at 0° hits at $x=3.93\text{cm}$, and at 30° at $x=4.37\text{cm}$.

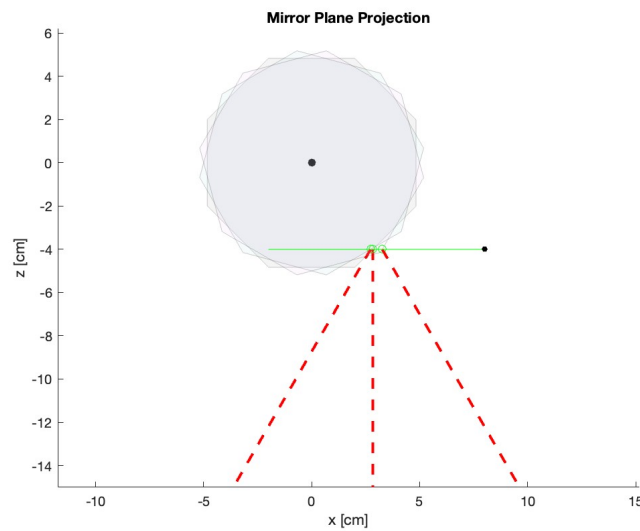


Figure 3.4: Simulated geometry of the light reflection from a polygon mirror using the parameters of model B. The beam at -30° hits the mirror at $x=2.73\text{cm}$, at 0° hits at $x=2.83\text{cm}$, and at 30° at $x=3.27\text{cm}$.

The next step for this model was to add an aperture. The only dimensions needed for this were the location of each side of the aperture with respect to the mirror's center. The z position parameters of the laser and, more importantly, the side length of the mirror greatly affect the ideal location for this aperture, as the physical location of the output beams will change. Figure 3.5 shows all these measurements, where R is the apothem of the mirror, z_{laser} is the z distance of the laser from the origin, and c and d the positions of each side of the aperture. A Maverick-specific measurement, the location of the D1 detector, e , is also shown in this figure. The aperture positions, c and d , must be adjusted to a reasonable location to allow the light coming off of the mirror actual exit the aperture. With all of these components, the MATLAB program could simulate system behavior.

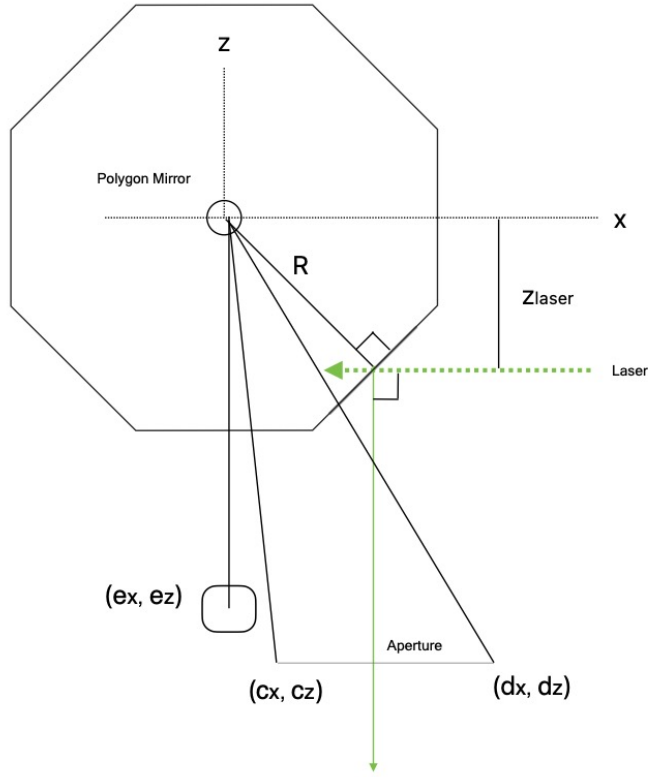


Figure 3.5: Required measurements within Maverick to create an accurate simulation.

The mirror rotates between a defined range of angles, and the points where the beam intersects with each end and the center of the aperture are marked. Figures 3.6 and 3.7 show the outcome of this process using the same A and B model parameters described previously, where in each case, an aperture of length $l = 3.5\text{cm}$ is 10cm away from the origin in the -z direction and is adjusted in the x direction so that the 0° angle directly exits the center of the aperture. Example A in Figure 3.6 allows angles from $\theta_{min} = -16.7^\circ$ to $\theta_{max} = 15.3^\circ$ to exit the aperture, while example B in Figure 3.7 allows angles from $\theta_{min} = -15.3^\circ$ to $\theta_{max} = 14.6^\circ$. Adding the aperture resulted in the same outcome as the previous model where having similar values of z_{laser} and side length seems to result in both a narrower, and more symmetric set of output angles. Given the limited number of examples explored, the exact nature and extent of this relationship cannot be defined yet, but it is certainly an important feature to keep in mind for future designs.

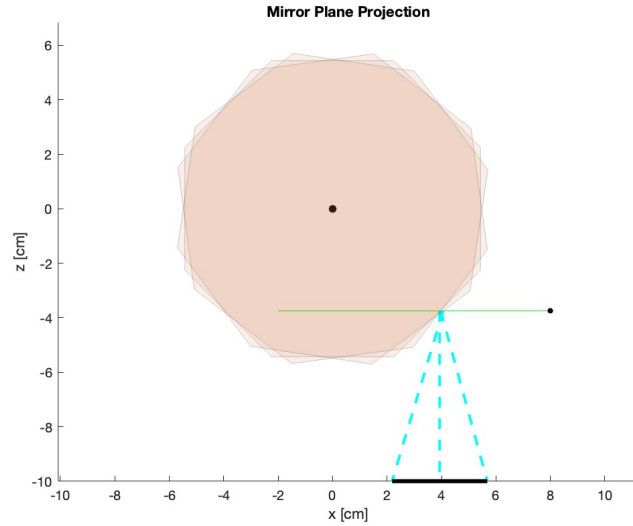


Figure 3.6: Adding an aperture to the simulation with the parameters of model A: $a = 4.5\text{cm}$ and $z_{laser} = -3.75\text{cm}$.

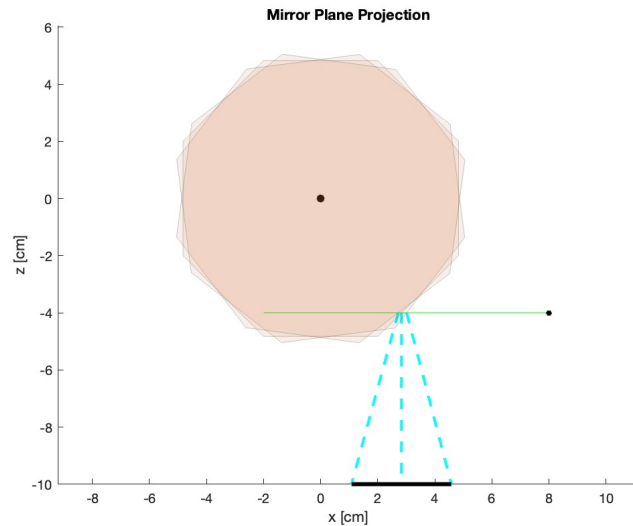


Figure 3.7: Adding an aperture to the simulation with the parameters of model B: $a = 4\text{cm}$ and $z_{laser} = -4\text{cm}$.

With a working general model, more specific parameters could be added to understand Maverick's particular scan plane behavior. The program also considered the D1 detector location for this analysis. The side length of the mirror and z position of the laser in Maverick are very similar, thus, as discovered within the general solution, the reflected angles have the more symmetric configuration where the 0° angle is central. However, from the specifics of the Maverick system, the $\theta = 0^\circ$ angle was not central to the aperture, but rather at an angle of $\theta \approx 1.8^\circ$, already disagreeing with the A2 assumption. The total output swath also exceeded the assumed 30° (A3), with a swath closer to 30.5° actually exiting the aperture. While there were not any previous assumptions about this, the program found the angle where the beam hit the center of the D1 detector to be $\theta_{D1} \approx -28.5^\circ$. These results are all shown in Figure 3.8. This model was extremely insightful in suggesting some possible issues with the initial assumptions on Maverick. However, all values discovered through the model are approximate; only unit-specific testing could provide accurate unit-specific values. Particularly for the D1 angle, due to the orientation of the detector, the center of the physical component is not necessarily the center of the detections. It is, however, the best possible approximation at this stage.

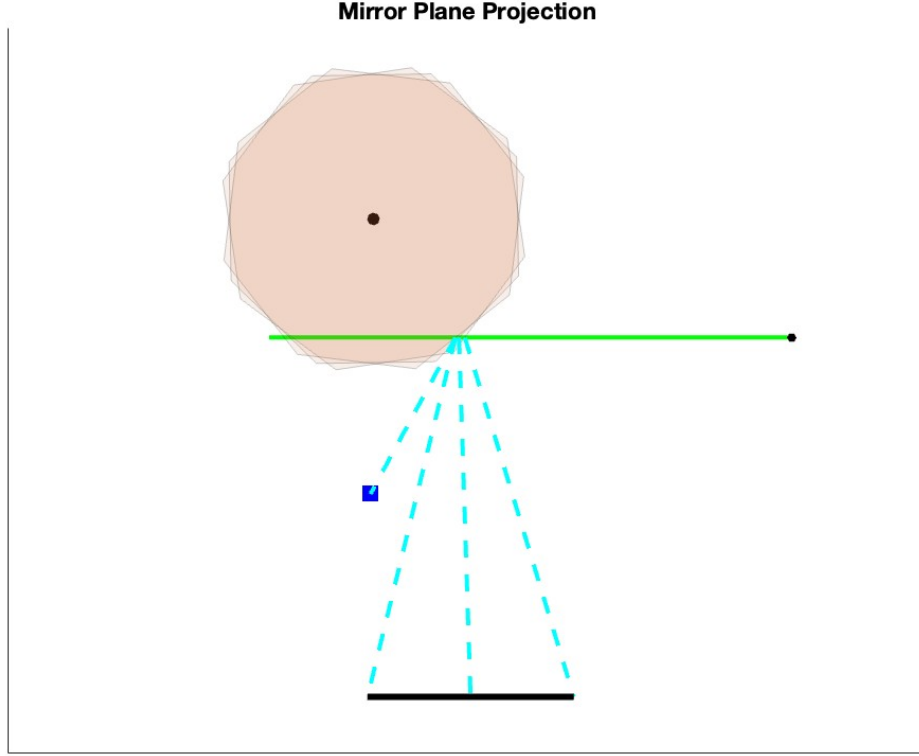


Figure 3.8: Model of significant output angles derived from Maverick system specifics, with the D1 detector added as the blue square.

The other behavior this model could analyze is how the light asymmetry, as shown in Figure 2.4, affects point placement within a point cloud. To do this, the real maximum and minimum pointing angles and laser positions as shown in Figure 3.8 were propagated to reach a simulated ground surface. The output distance of these laser paths and their return distance were calculated and translated to a time to accurately reflect the information that Maverick would interpret in this situation. Then, a second scenario was added to this analysis to reflect how this information would be processed. Using the same central angle of $\theta \approx 1.8^\circ$ and the same swath size of 30.5° , a symmetric cone about the central axis at 1.8° was plotted, and the beams at maximum and minimum pointing angles propagated to meet the time information for the previous scenario. The

actual point of detection, and point of assumed detection, could then be compared. The outcome was that the distance between these two points, the real and assumed, was less than 1mm. Figure 3.9 shows a zoomed-out and up-close view of this. Figure 3.9a shows that the shape difference in the real, asymmetric configuration and the symmetric one becomes very difficult to see even when the ground is only 1m away. More quantifiably, Figure 3.9b shows that despite the small difference, the point placement error is less than a millimeter. Other sources of error, as discussed in Section 1, cause more uncertainty than this. Thus, the effects from this asymmetric beam translation are deemed negligible and unnecessary to correct in processing.

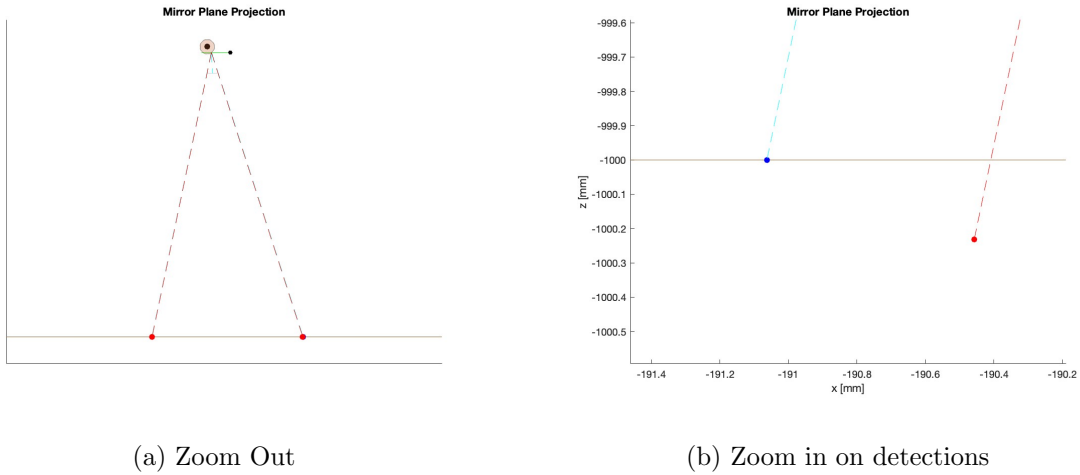


Figure 3.9: Modeling the expected detection assuming a symmetric cone vs actual point placement given the known offsets.

3.3 Computational Pointing Improvements

3.3.1 Defining an Algorithm

With a well-defined model of the system, the next step was to analyze how well the model agrees with empirical Maverick measurements. A few tests were designed to measure the central angle offset and D1 angle, the output scan, and the angle distribution within a single swath. Before testing, however, a point cloud was processed using all assumptions to provide a basic understanding

of scan behaviors as a reference for further improvements.

In a basic processing model, only D2 detections need to be analyzed, as in addition to the previously stated assumptions, there is an additional simplification that expects an entire swath to be scattered back towards the unit and detected every scan. Consequently, a program needs to find the time record for the middle and each end of a swath, then simply uses that information to assign -15° and 15° at each end, and 0° in the middle. This processing is challenging to automate but can be executed and evaluated. Figure 3.10 shows the results of this processing method presented in the form of a point cloud. For clearer viewing, no water is present in this data set; it is purely topographic. While this cloud does have a generally expected shape and elevation, there is significant unevenness between flight lines. No distinct features can be found suggesting there are issues with the assumptions, per model results. This same data set is shown throughout this chapter to illustrate the improvements in processing. Note that this and all subsequent data sets have undergone a GPS PPK correction. Figure 3.11 shows the distribution of z values in this cloud, as well as a CloudCompare[3] generated gaussian fit with a full-width half-max (FWHM) measurement of 0.506m.

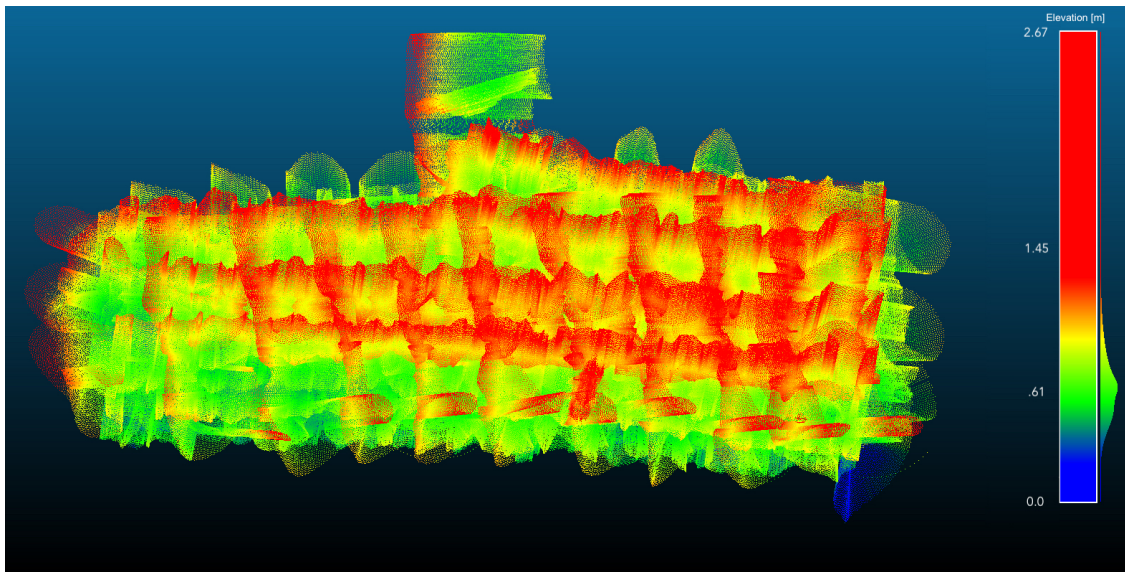


Figure 3.10: Experimental point cloud that has been processed using poor assumptions as described above.

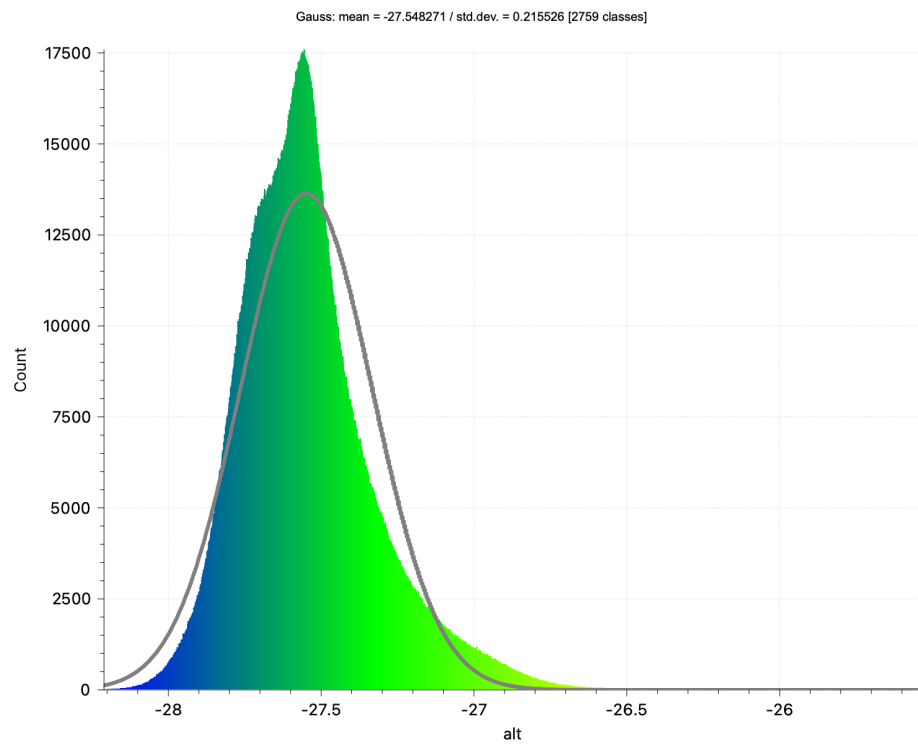


Figure 3.11: Gaussian distribution of elevation values for the cloud displayed in Figure 3.10.

For a more advanced computational model, three important pieces of information required measurement: the central offset angle, θ_{off} , the D1 angle, θ_{D1} , and the size of FOV exiting the aperture. The computational concept of this updated algorithm uses a moving window averaging analysis. The program analyzes a fixed number of received time records, a window, within each loop and gradually steps through all records with a fixed number of records step size until all the data has been parsed. The program analyzes all the detections within each window as it steps through. The program calculates time weighted averages of records depending on how many of a specific detection exists within a window compared to the total number of detections to find the middle of each D1 and D2 detection group. At the middle of the D2 detection window, the calculated offset angle, θ_{off} , is assigned to the detection. Per assumption A1, there is an even distribution of pointing angles between that offset and the middle of the D1 detector where $\theta_{pointing} = \theta_{D1}$. Eq 3.1 assigns them as such. In this equation, T is the time the detection in question was received, t_0 is the time at the center of the aperture, and ΔM is the time between the center of the most recent D1 hit and the center of the aperture.

$$\theta_{pointing} = \frac{T - t_0}{\Delta M} \theta_{D1} + \theta_{off} \quad (3.1)$$

3.3.2 Measurement Tests

The first test designed for this study was a physical measurement of Maverick's output angles. This initial test was deemed exploratory and thus not conducted under typical, stringent experimental procedures. Particularly, there was one major flaw: the test could not be performed with the same unit that took the original field data. Inherent uncertainties within every unit, such as optical alignment errors or manufacturing tolerances, may cause slightly different behaviors. Nonetheless, the desired outcome of this test was to provide better understanding of the values compared to those calculated in the model.

The first step in performing this test was orienting an incomplete tabletop unit in a controlled lab environment so the laser reflected on a flat wall surface. The tabletop unit had no aperture

attached, so each part of the 90-degree scan created by the PM facets appeared on the wall. With proper personal protective equipment (PPE), the laser was turned on and the mirror rotated through the scan. Each end of the scan could be marked on the wall, as well as where the laser became blocked by the D1 detector. Then, the aperture was added to the system to mark each end of the swath. The last measurement to perform for this test was simply a perpendicular line between the center of the aperture and the wall. That center point was $x=0$, and all other measurements had a relative distance to that point. Figure 3.12 shows a diagram of this experimental setup.

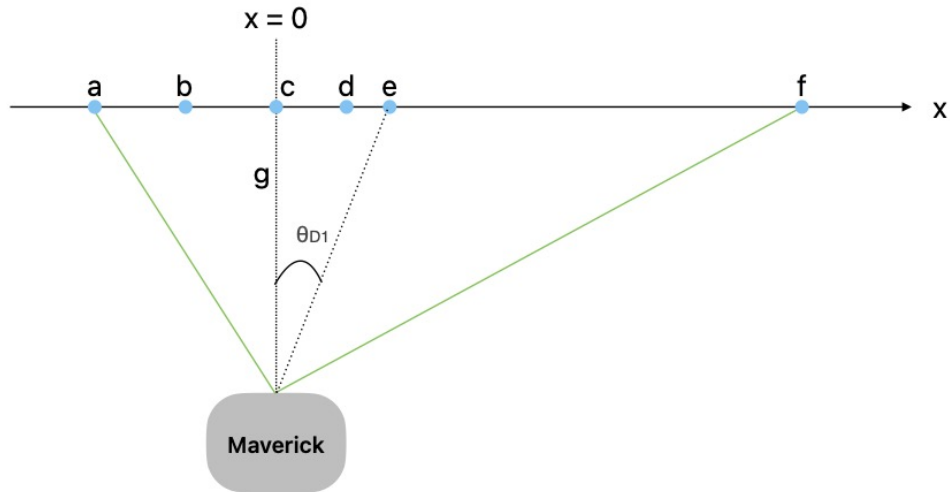


Figure 3.12: All measured distances in the wall measurement test. Points a and f are each extreme end of the scan, where negative angles are on the side of a and positive on the side of f. Points b and d are where the scan was cut off by each end of the aperture. Point e is where the scan was cut off by the D1 detector, and point c is the direct horizontal point to the center of the aperture. Line g indicates the distance from that point c and the center of the aperture.

In Figure 3.12, all angles are relative to the straight line at $x=0$ from the center of the aperture to the wall, marked as point c in Figure 3.12. All points to the right of c are negative angles (d-f), and to the left are positive (a,b). According to assumption A2, if the central angle

was 0° , the distance between that point and each end of the aperture should be symmetric. This was not the case - the distance between points c and b is larger than the distance between points c and d, suggesting a positive angle offset, which does align with the model. The exact value of this offset, however, worked out slightly different than the model, measuring at $\theta_{off} \approx 1.5^\circ$. The measured D1 angle was $\theta_{D1} \approx -25.5^\circ$, a significant 3° difference from the -28.5° found by the model. On the other hand, the total swath size was 30.5° , exactly agreeing with the model. Figure 3.13 shows a zoomed in view between points b and d on Figure 3.12. This shows the physical properties of how the central angle is offset, since the line labeled h represents where the 0° line is compared to the directly vertical central line g.

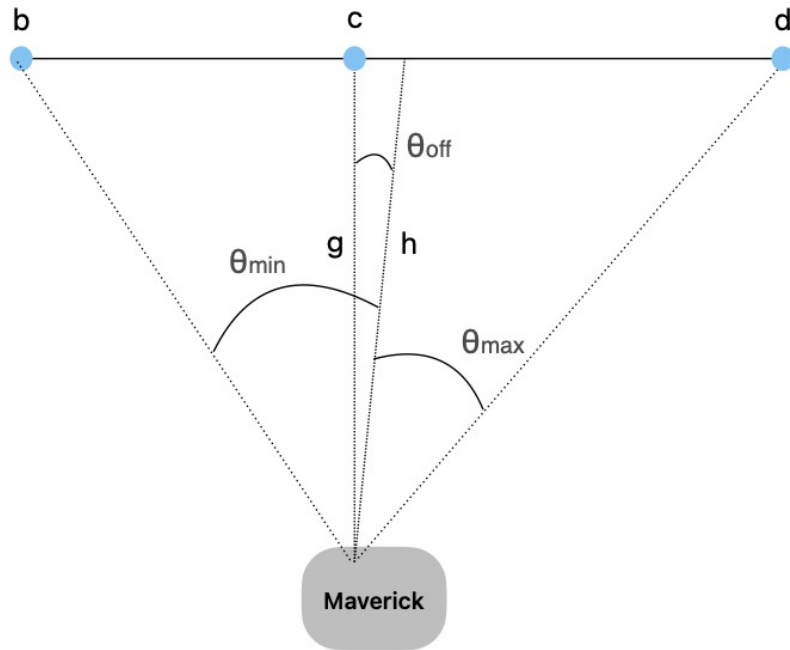


Figure 3.13: Zoomed in view showing the angles exiting the aperture and the offset angle in the wall test.

Figure 3.14 shows the results of applying the algorithm defined by Eq 3.1 with the calculated

angle values. Due to the differing nature of the computations in this cloud and the previous cloud shown in Figure 3.10, it is complex to quantify the improvement of this algorithm's changes. However, there are a couple of obvious improvements, including a simple reduction in visual noise and the less apparent drone flight paths. These improvements are also visible in the histogram shown in Figure 3.15 that describes the z values in each image. In the more recently processed cloud in Figure 3.14, the variance in this histogram is clearly smaller than in Figure 3.10, with the FWHM almost reduced by half to 0.272. A perfectly processed data set is not expected to be a perfect histogram due to the natural fluctuations in the surface elevation, however, a sharper histogram does indicate processing improvements by reducing the extraneously placed points. Additionally, the lack of ground control points in this data set makes it difficult to define an x-y improvement metric, but the improvement in z can be analyzed. There are a couple of misaligned individual swaths circled in blue, but it is promising that those are visible and not hidden by the variations in the bulk of the cloud. There are also a few distinguishable targets, one boxed in pink and one in purple. For this result, it is only important to note that they can be distinguished, which was not the case in the initial point cloud.

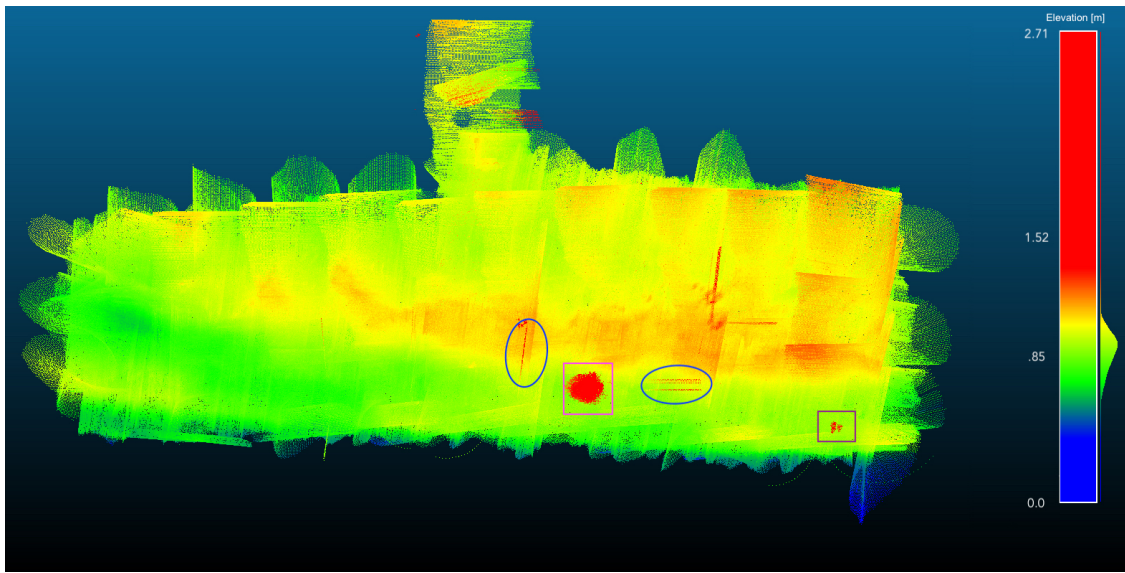


Figure 3.14: Reprocessing of the same point cloud shown in Figure 3.10 using the angles from the wall test.

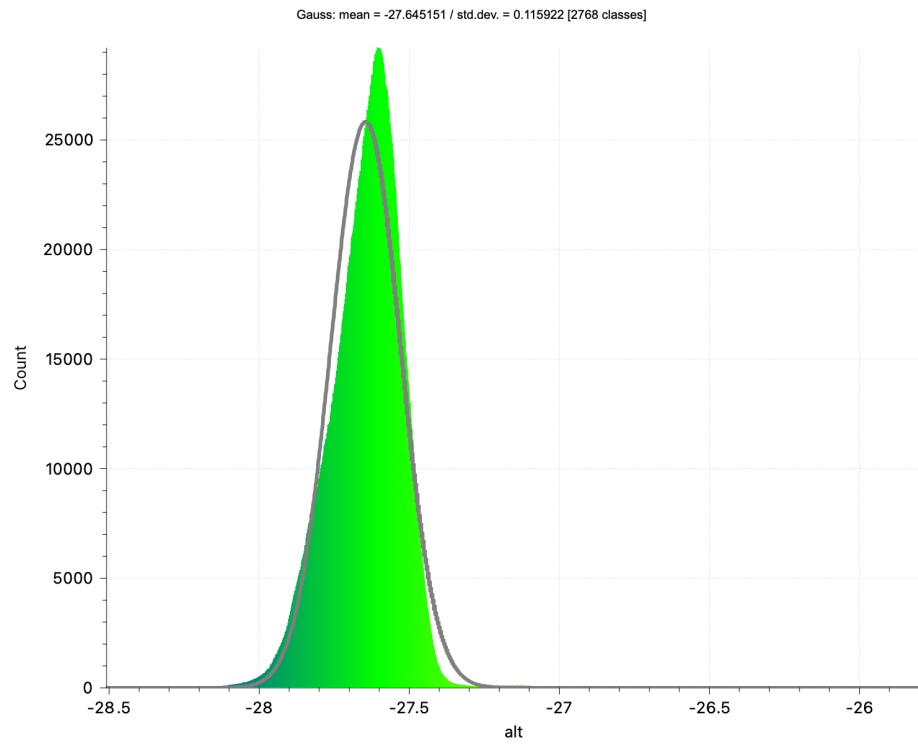


Figure 3.15: Gaussian distribution of elevation values for the cloud displayed in Figure 3.14.

The goal of the subsequent test was to more rigorously calculate the central offset angle using a fully built unit. Particularly, in this case, the same unit used to collect the field data as presented in the point clouds. The general concept of this test is that if the unit is facing a flat surface and the unit is parallel to that surface, the beam's path when it exits the unit with an angle of 0° should be the shortest path, and therefore the least time of flight, to the wall.

To perform this test, the following procedures were followed:

- (1) Add a neutral density 1.8 (ND1.8) filter to the aperture of Maverick.
- (2) Place the unit on a steady surface so its back is against one wall and it is facing the other side of the room.
 - (a) Ensure the back of the unit is flush with the wall surface to remove any skewed data from a unit rotation.
 - (b) The wall the unit is facing should be empty in the area the laser will reflect on.
- (3) Don proper PPE for laser observation.
- (4) Turn on the unit.
 - (a) Ensure the whole swath is only seeing the flat wall that it is facing.
- (5) Continue data collection for approximately 2 minutes.
- (6) Turn off unit to end data collection and complete the test.

This test was performed in a small room with white walls. Given Maverick's typical operating conditions of flying at 30 meters with a variable surface, the ND filters were necessary to attenuate the much stronger signal than it typically receives. Specifically, the length of this room in the direction that the unit was collecting data is 1.5m. This distance means, given the $\approx 30.5^\circ$ FOV, the area needed for the whole swath on the wall was also approximately 1.5m.

With the measurement of this data complete, the travel times could be analyzed in conjunction with the mirror angle to determine if an offset is present. Figure 3.16 shows the collected

data, where the y-axis represents travel time, and the x-axis represents the clock time. This figure focuses on three swaths, defined by a characteristic U shape, reflecting the expected behavior of the stationary laser scanning across a flat area. One initial finding that is clear about these swaths is the general asymmetry of the U shape. The right side appears to rise higher (have longer travel times) than the left side, further suggesting the existence of a positive central angle offset. Additionally, on the right side, there seems to be a strange curl away from the otherwise consistent U shape. This was determined to be a product of receiver capabilities and is discussed further in Section 5. Generally, the minimums of these Us represent the shortest travel time, thus, the 0° pointing angle should directly intersect them. This concept is consistent with the theory discussed to design this test.

Figure 3.16 shows the same U plot but with additional pointing angle information provided by the designed processing algorithm. The program created to display these plots will draw a line through the assigned 0° pointing angle using minimum value finding to observe how aligned it is with the minimum of each travel time. An accurate offset would appear as a vertical line perfectly bisecting the minimums. Figure 3.17 shows two examples of this, one with 0° offset and one with the optimal $\theta_{off} \approx 1.7^\circ$, sitting in-between the modeled value, and the value from the first test. Given the more stringent nature of this experiment, this value is more accurate than by other measures. Analyzing the resultant point cloud data can verify this claim.

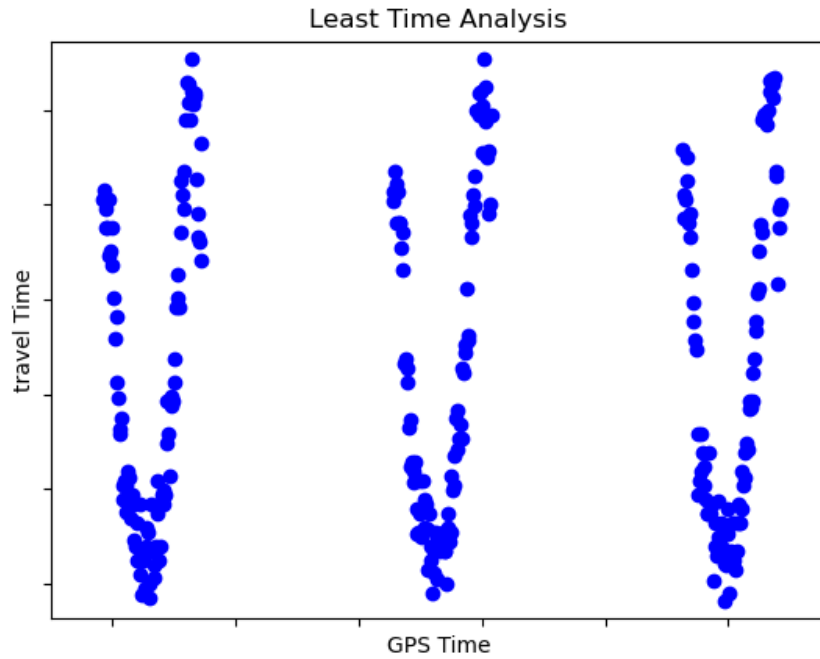


Figure 3.16: Collection of detections made by Maverick and their recorded travel times from output to reception.

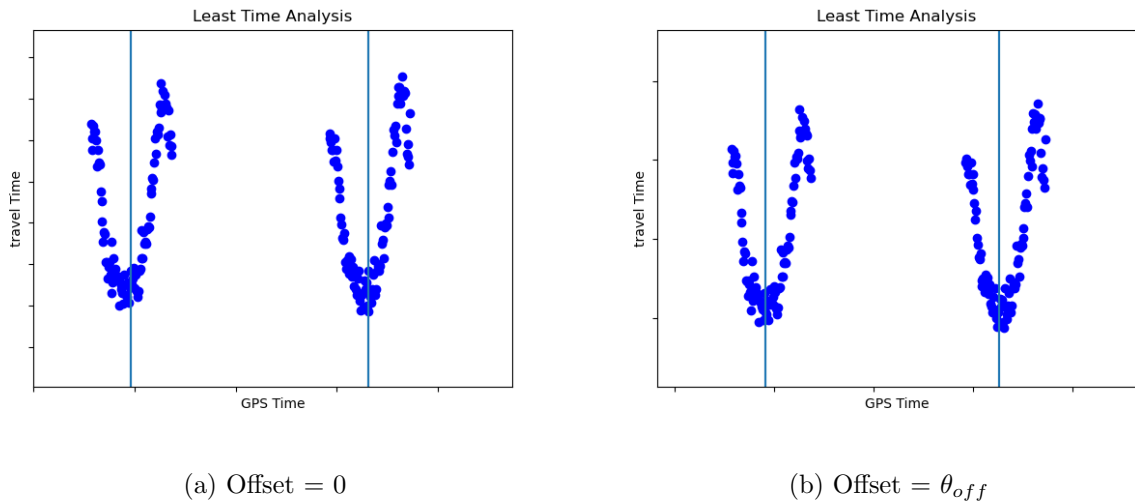


Figure 3.17: Adding where the 0° angle was placed within a swath as compared to where it should be - at the smallest travel times.

The same algorithm used to process the cloud in Figure 3.14 was used for this processing, making the two relatively straightforward to compare. Figure 3.18 shows the point cloud with this new offset, and a few visual inspections immediately stick out. The first is the smoothing of the background surface, most notable in the top right corner of the cloud. The object boxed in pink in the first image also sharpens with this new offset. The mis-rotated swaths do not seem to change, but this is an expected result as changing only the offset should have no effect. Once again, the FWHM of the gaussian shown in Figure 3.19 reduces from the previous cloud to 0.258m, quantitatively suggesting smoothing out of the data.

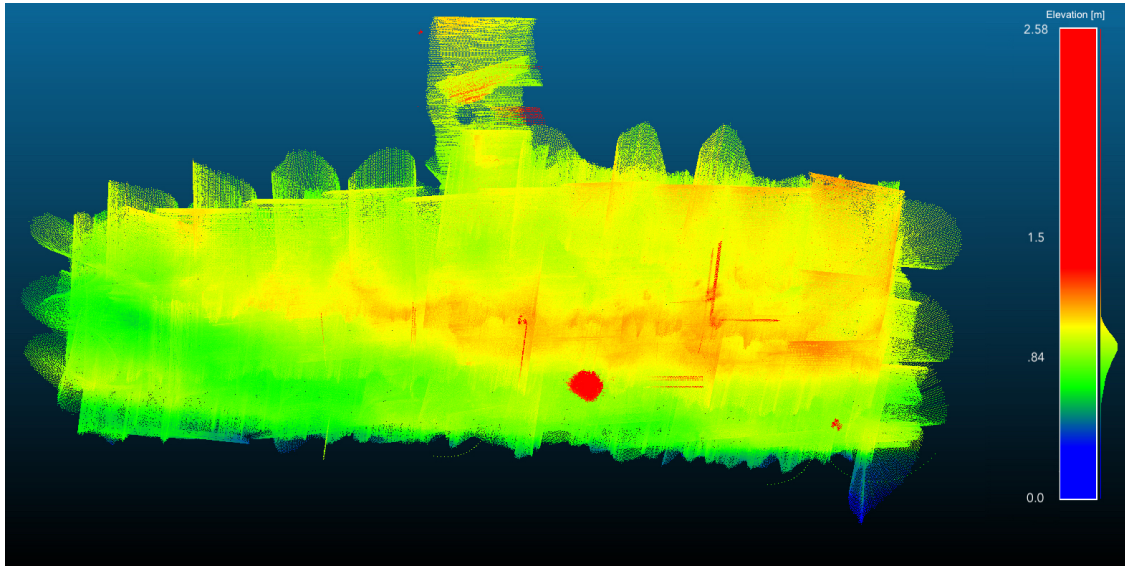


Figure 3.18: Next point cloud reprocessing using the offset from the least-time test.

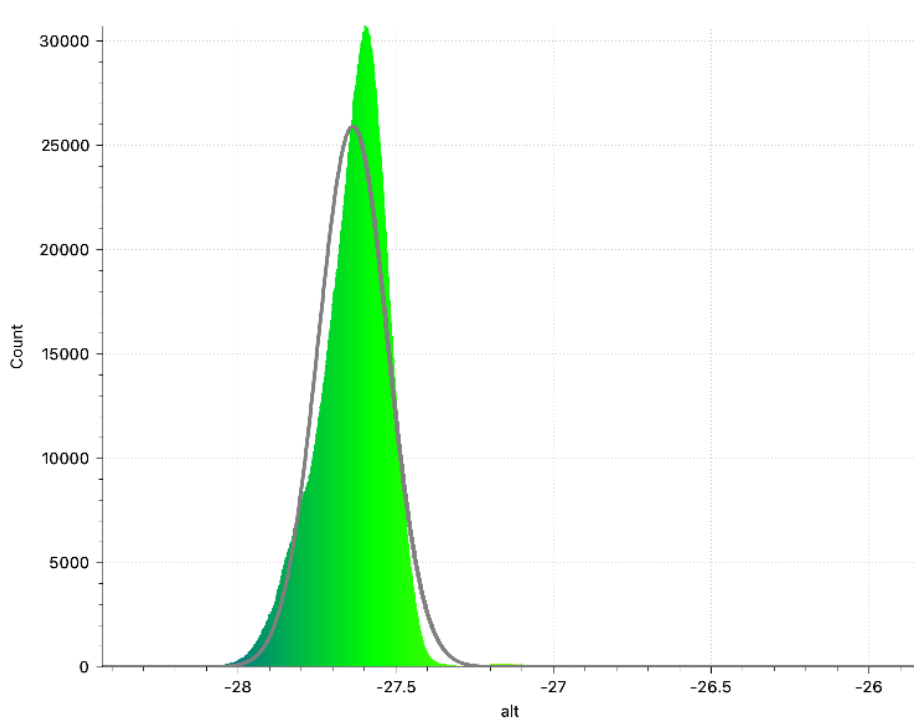


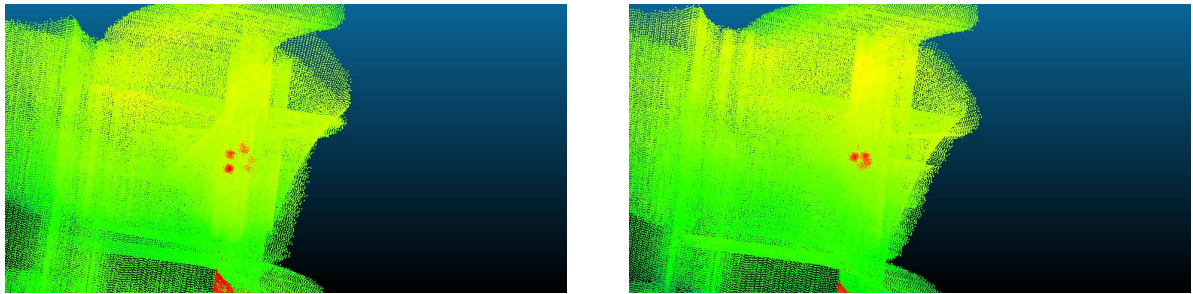
Figure 3.19: Gaussian distribution of elevation values for the cloud displayed in Figure 3.18.

3.3.3 Boresighting

One thing that has yet to be discussed but is essential within the context of pointing angles is boresighting errors. Boresighting errors stem from a misalignment of the LiDAR body and the IMU coordinate frames. In prior data processing techniques for Maverick, the flight line misalignment in the point cloud from not accounting for an offset would not have remained in a final product. Instead, this offset error would be misdiagnosed as a boresight error, and fixed via a boresight correction. Boresight corrections use an added offset to a unit's pitch, roll, and yaw to amend this misalignment. So, while this offset could technically be corrected, it was done so in an incorrect manner by giving a rotation to the IMU coordinate frame rather than properly aligning the pointing angles within the body frame. A full characterization of pointing angle error requires de-coupling of these two different error sources.

Figures 3.20a and 3.20b show a zoomed-in cluster of points. All these protruding points

are from the same object, but were scanned by Maverick at different points in the flight. These figures are from a different data set than the one in the prior point clouds, but show the same scene with the same object as the one shown boxed in purple in Figure 3.14. In Figure 3.20a, the cloud processing used a 0° offset, and Figure 3.20b used the least-time test calculated offset $\theta_{off} \approx 1.7^\circ$. These points are much closer together when processed with the proper offset than with zero offset. This outcome makes sense as the primary consequence of an incorrect offset is systematic mis-rotation within the point cloud. Both a pitch and roll boresighting correction are necessary to align this data with a 0° mirror-pointing offset. However, only a small pitch correction will align the data after adding the correct mirror-pointing offset. Figure 3.21 shows this point cluster's final, boresighted image.



(a) Cluster of points that are all the same object seen in red when a 0° offset angle is used.
(b) Cluster of points that are all the same object seen in red when θ_{off} is used.

Figure 3.20: Boresighting Demonstration

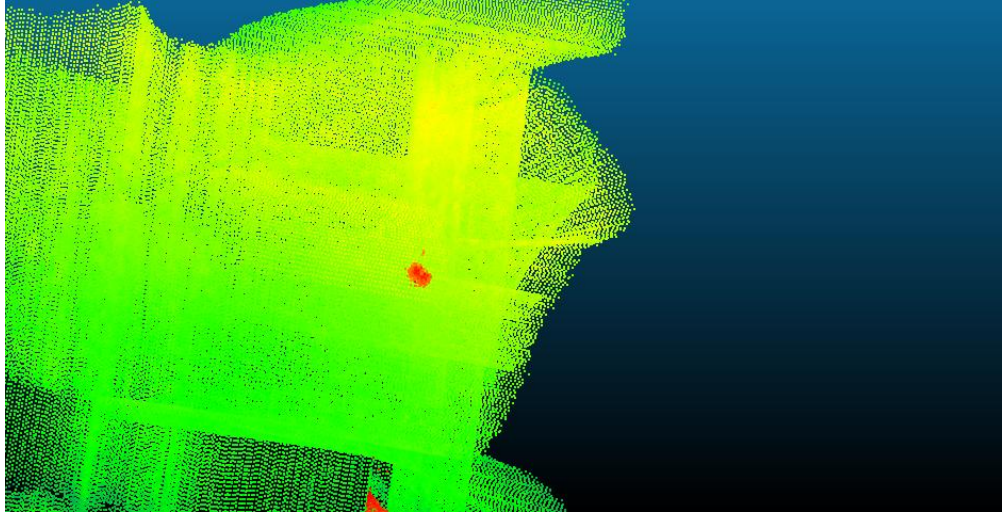


Figure 3.21: Same cluster of points shown in Figure 3.20 when the point cloud is fully boresighted.

3.3.4 Calibration

The next step towards understanding the pointing of this system was to evaluate the pointing angle of the beam at the D1 detector. Based on the data processing Equation 3.1, the physical effect of this value being incorrect is systematic stretching or compressing of the points in each swath, depending on if the angle is estimated to be too large or too small. Figure 3.22 illustrates this effect. The practical reason for this is that assigning the detector an angle smaller than what it is shifts the $\pm 15^\circ$ boundary closer to the center than it should be. To test the extent of this swath size manipulation and the accuracy of D1 angle calibrated targets are compared to their known sizes.

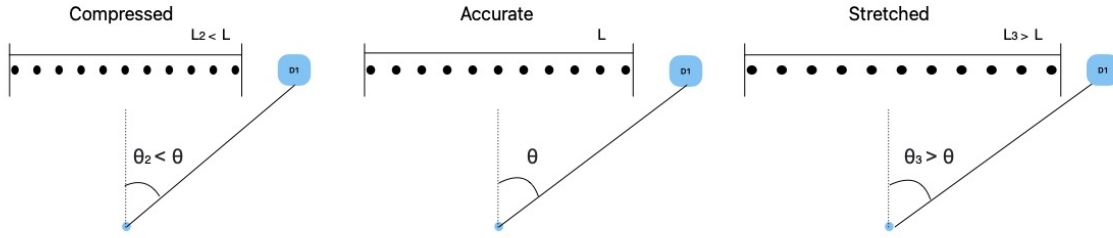


Figure 3.22: Stretching or compression effects of having an incorrect D1 angle.

Figure 3.23 shows a bird's eye view of a calibration cross target (CCT). At least one CCT is present in all this thesis' data sets. With accurate pointing information, the CCTs in the point cloud should reflect the dimensions in the figure. Given that the side lengths of the CCT are both 1.64m, a diagonal length of 2.316m is expected. As shown in Figure 3.24a, this is not the case when using the D1 angle calculated in the first experiment of $\theta_{D1} = -25.5^\circ$. Adjusting this value to stretch the points to meet the dimensions of the CCT better returns a D1 angle closer to -27.0° , shown in Figure 3.24b. Interestingly, with an even higher angle to allow the CCT to match the real dimensions more accurately, the cloud becomes less smooth. To balance the smoothness and CCT dimensions, -27.0° was discovered to be the optimal angle. Figure 3.25 shows the whole point cloud processed with this optimal angle. Figure 3.26 shows the histogram and gaussian fit for the z values in this cloud, where the FWHM slightly reduces from the previous cloud to 0.257. This slight decrease comes from a general reduction in misplaced points from the compression. Furthermore, this cloud's most significant visual update is a general stretching of points in the horizontal direction.

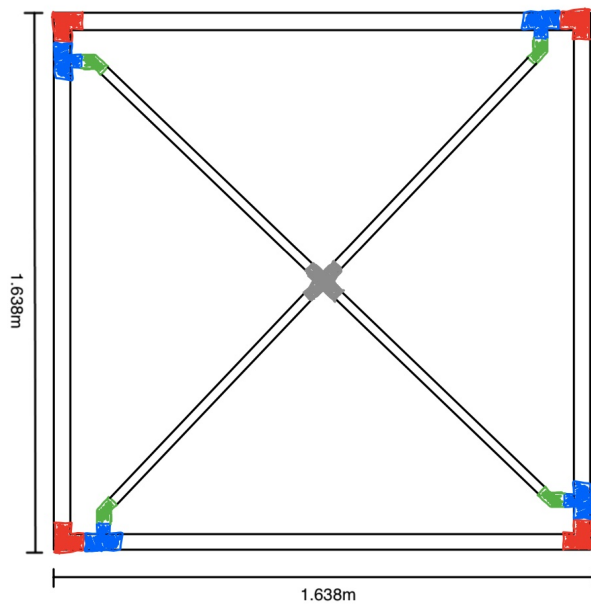
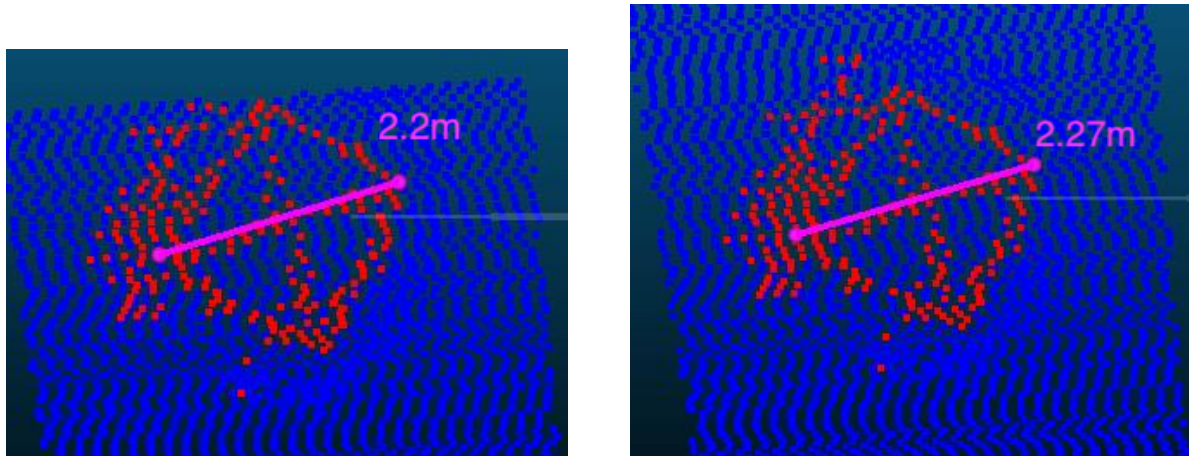


Figure 3.23: Dimensions of a real cross calibration target that is scanned by Maverick.



- (a) Diagonal size of a CCT when a D1 angle of -25.5° is used.
(b) Diagonal size of a CCT when a D1 angle of -27° is used.

Figure 3.24: CCT apparent dimensions using different D1 angles.

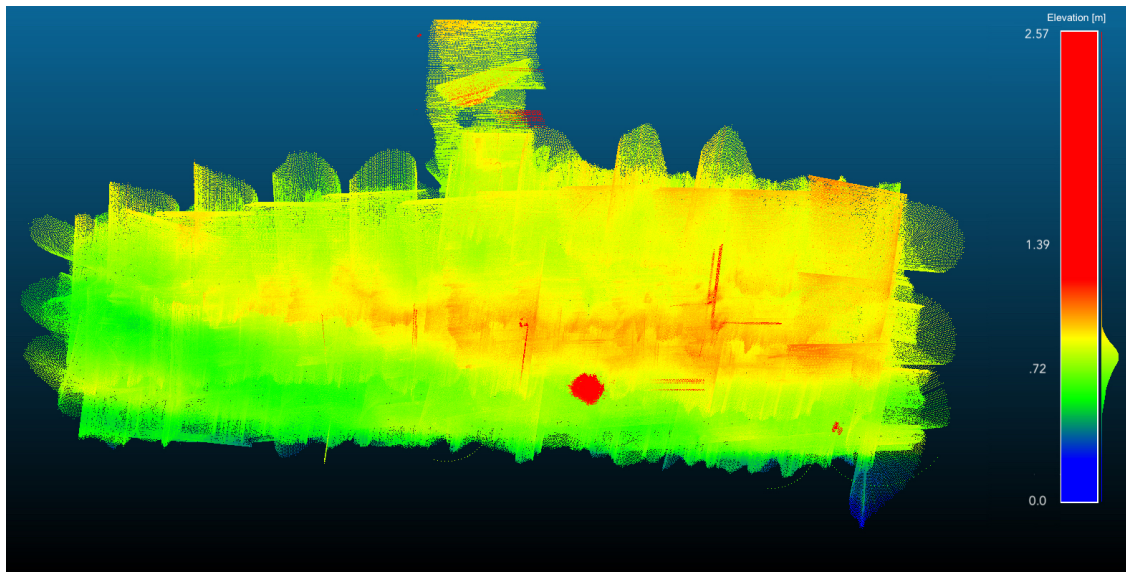


Figure 3.25: Reprocessing the point cloud using the updated optimized D1 angle.

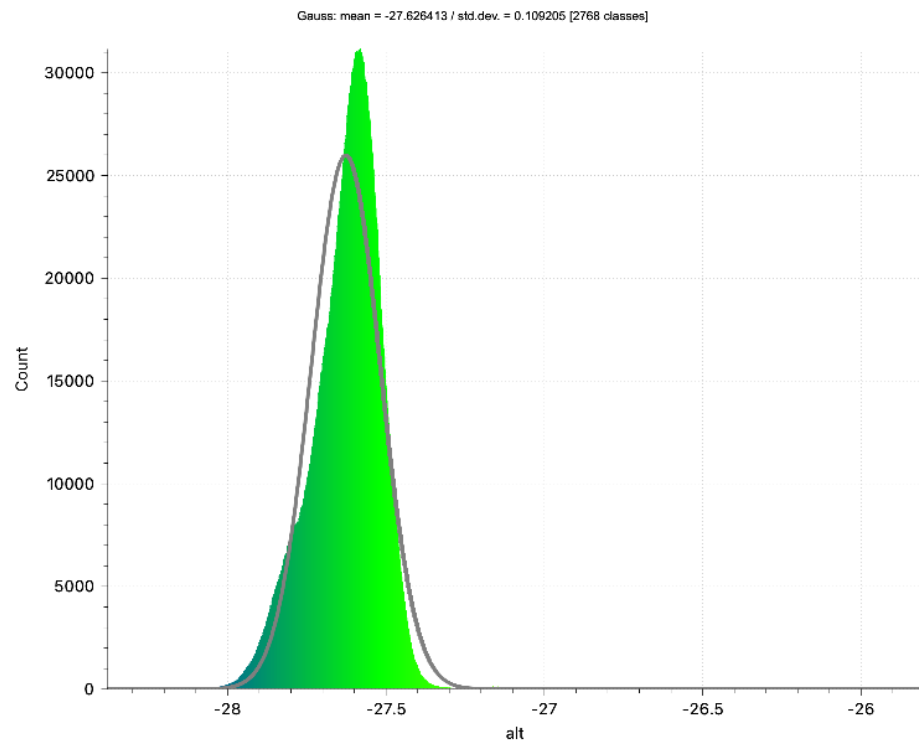
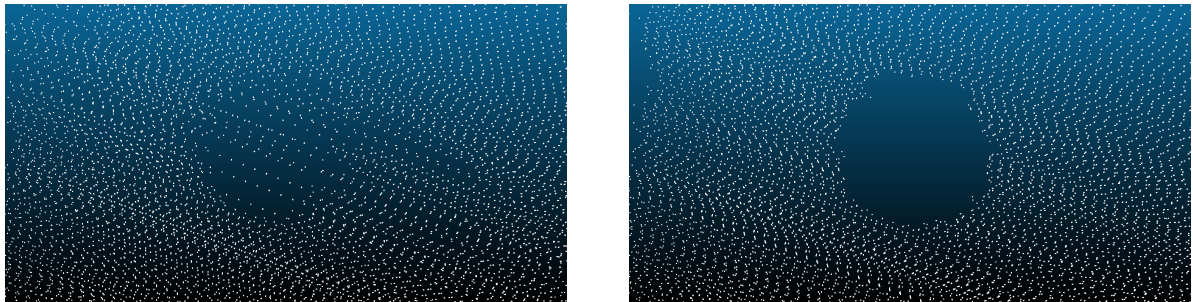


Figure 3.26: Gaussian distribution of elevation values for the cloud with an optimized D1 angle displayed in Figure 3.25.

3.3.5 Averaging and Error Analysis

The current collection of tests has significantly improved pointing knowledge, specifically related to the central offset angle value, the D1 angle value, and how those two components relate to the initial A2 and A3 assumptions. However, there has not yet been any mitigation of individual swaths that appear to be mis-rotated from the greater scene. Figure 3.14 has these swaths circled, but they remain present in subsequent point clouds. This issue goes back to the simplification discussed at the beginning of this section - that the entire swath of signals is received. While this simplification did allow for improvements in pointing knowledge and the data processing that stemmed from that, if not addressed it can cause other issues that can hinder further progress. In addition to these protruding swaths, there is another area near the takeoff where these effects are evident. The UAV takes off from a circular landing pad made of a very absorptive material. The purpose is so the light doesn't reflect at those low distances and overwhelm the receiver. It also means that there should be a circle with no points around the takeoff area. Figure 3.27a shows an image of what this circle looks like using that simplification.



(a) Obscured point collection of the circular landing pad due to center swath misplacement.
(b) More clearly defined landing pad due to the addition of averaging.

Figure 3.27: Takeoff Area

Assumption A1, that the angles are evenly distributed within a scan, can be used to dispose of the simplification that the entire swath of signals is received. One bearing of this assumption is

that, given this even distribution, the ratio of the time it takes for the mirror to spin between the D1 and D2 detectors and then from the D2 detector back to D1 should remain constant. This ratio is shown physically in Figure 3.28 which visually describes the distance the laser is spinning for each time period. If the PM mirror velocity remained steady throughout a flight, this assumption would be even more straightforward, as those times should not change. However, prior to any research done for this thesis, mirror drift throughout a flight had been demonstrated. Even with that drift, the ratio values should remain consistent throughout data collection, even though the times do not.

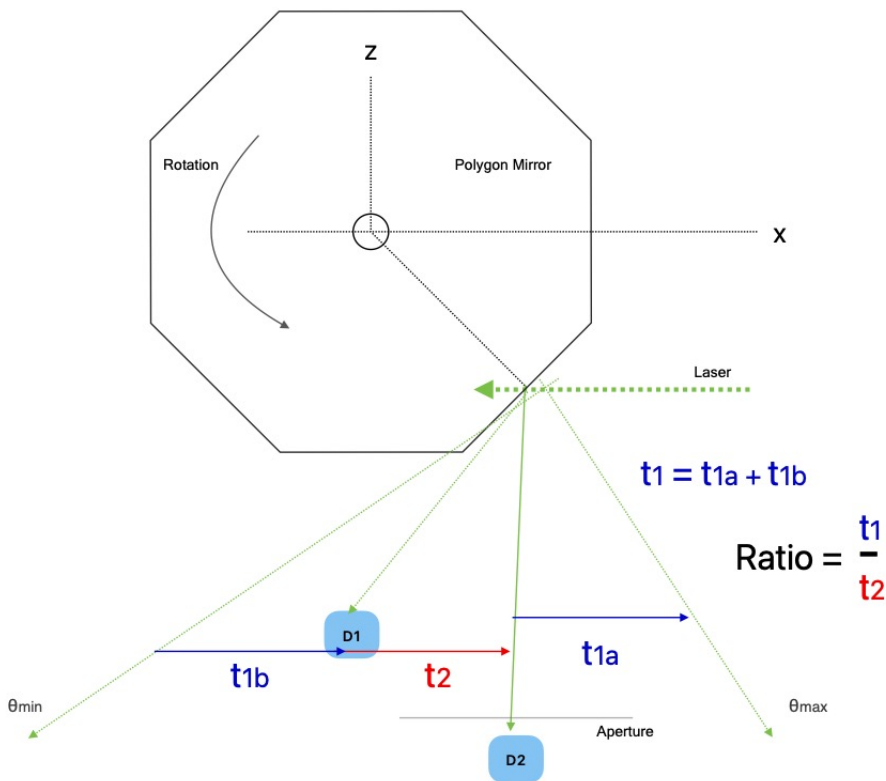


Figure 3.28: Physical description of the time ratio that should be consistent throughout data collection. t_1 is the time between D2 and D1 and t_2 is the time from D1 back to D2.

A new processing algorithm uses this average ratio value to determine the center of each

swath. This process means that the program will not inherently misidentify the center when the swath is incomplete. With the previous simplification, if part of a swath did not get any returns, the program would misidentify the placement of that central angle θ_{off} , which led to those individual swath mis-rotations, and misplacement of swaths seen on the circle. Figure 3.27b shows the same takeoff pad area with this updated processing code. The circle is much clearer here.

One common reason for these cut-off returns is when flying over water, if the surface is perfectly smooth, it will behave like a mirror and reflect the light in a specular manner away from the LiDAR receiver. A smooth ground surface could also behave this way under the right conditions. Most of the time, scattering surfaces will have enough roughness that the light reflects more diffusely, allowing the system to detect this reflection. However, the specular reflections occur often enough that processing must account for them. Figure 3.29 illustrates the difference in these types of reflections.

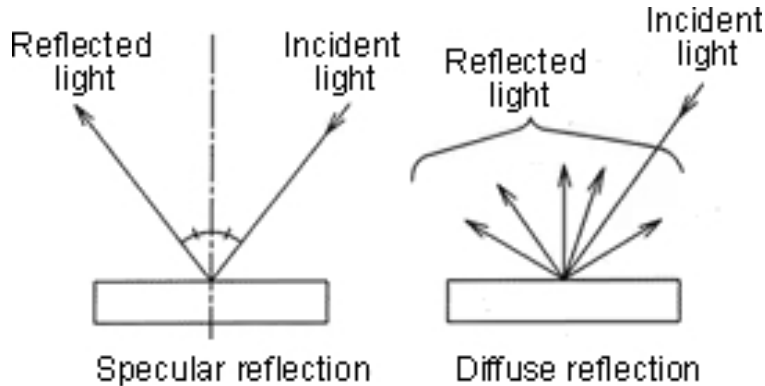


Figure 3.29: Different types of reflection [10].

Figure 3.30 shows the fully processed cloud using this averaging method. The FWHM of the gaussian fit for the histogram of this cloud as shown in Figure 3.31 shows another very slight reduction from the previous cloud to 0.255, a promising but somewhat insignificant indication of improvement when analyzing only the z-component. However, there are also horizontal components not captured by the FWHM analysis that appear as the circular takeoff pad improvement shown

in Figure 3.27b, and the objects boxed in Figure 3.14 now appear much sharper. The singular misrotated swaths that have been present in all clouds thus far now align with the rest of the scene. The background is generally much smoother, as well. Thus, visual results indicate the processing is working well.

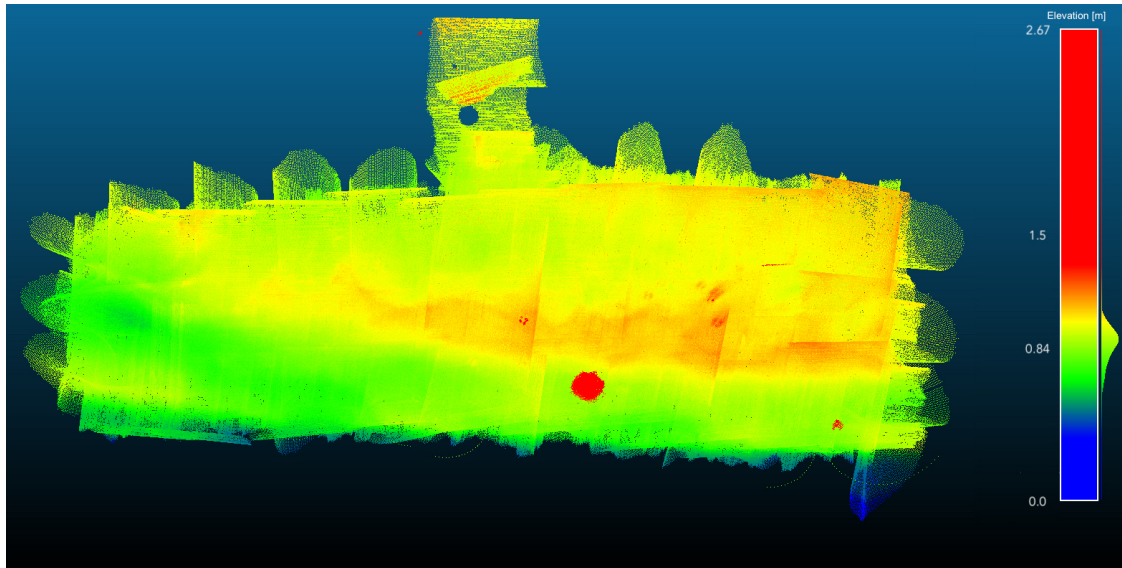


Figure 3.30: Reprocessed point cloud but with the addition of averaging to find the central swath points.

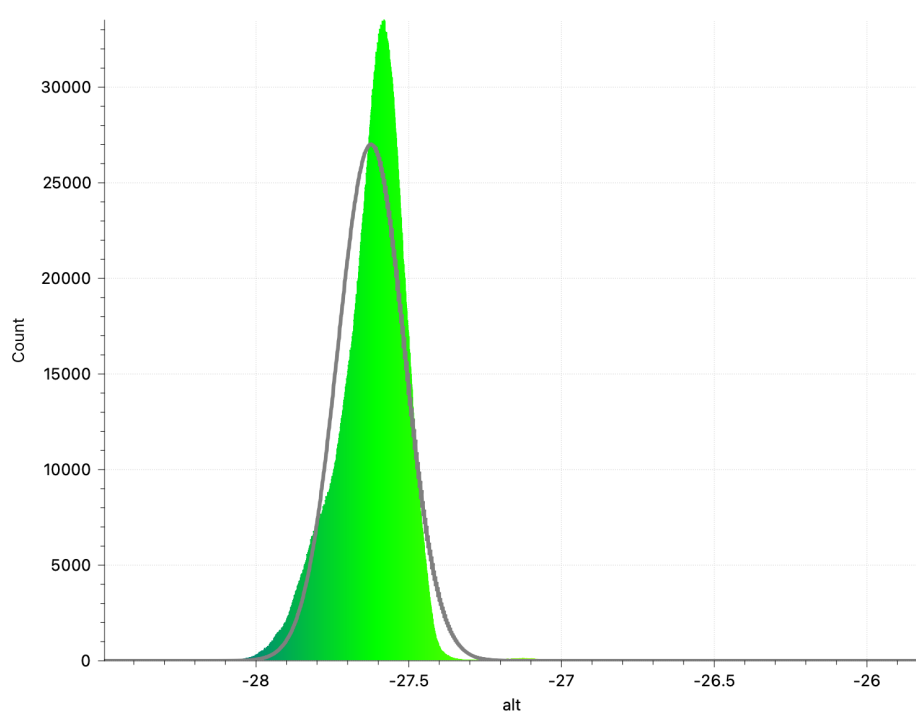


Figure 3.31: Gaussian distribution of elevation values for the cloud with averaging added displayed in Figure 3.30.

Calculating the error in this ratio was difficult due to its single-pass nature. A simple option would have been to save a list of all the ratios and perform statistical calculations. However, Welford's algorithm described by Eq 3.2 provides a numerically stable method to compute the variance of a variable x using just a single pass of data [13] for computational efficiency. From an analysis of a couple of data sets, the average ratio was approximately $R = 2.2$. Given that the time ratio between these areas is equal to the angle ratio, and that the full scan spans 90° , the system of equations outlined in Equations 3.3 and 3.4 are used to calculate the angles spanned in each of these periods. θ_1 is the close angle between the first D1 detector hit, and the center of the aperture, and θ_2 is then the angles spanned between that center hit and the contiguous D1 hit. These values suggest that the angle of the D1 detector is -27.0° , matching the optimal value discovered using the calibration targets.

$$\sum_{i=1}^N (x_i - \bar{x}_N)^2 - \sum_{i=1}^{N-1} (x_i - \bar{x}_{N-1})^2 \quad (3.2)$$

$$\theta_1 = R\theta_2 \quad (3.3)$$

$$\theta_1 + \theta_2 = 90^\circ \quad (3.4)$$

The other result from this analysis was that the standard deviation of this ratio was 0.1. Numerically, this result means that within one standard deviation, each pointing angle the swath might shift within approximately $\pm 1^\circ$ of what is expected. This difference can certainly manipulate the data as demonstrated in Figure 3.22. This result can mainly be attributed to two things. The first is simply errors in computational averaging. These errors typically stem from the same incomplete swaths that made averaging necessary and appear as additional variance in that ratio. The other reason is likely that this ratio is genuinely less consistent than previously expected. This result is extremely important for error characterization, however, implementing mechanical solutions for this issue was not within the scope of this research. Section 5 does explore and discuss possible mechanical solutions for future implementation.

Despite the non-ideal outcome of this error analysis, the averaging method, with the discovered θ_{off} and θ_{D1} pointing angles, was still determined to be the best solution created for this thesis. The only step left within processing was to apply the pitch boresight correction. With that complete, the final point cloud is shown in Figure 3.32. The algorithm used for this boresighted data is the same as used in Figure 3.30. The FWHM of this new cloud does display a tightened FWHM from the previous step to 0.251, as shown in Figure 3.33. Visually, this cloud also has the smoothest background surface thus far, implying that all flight lines are now properly aligned, the expected result of a proper central offset angle and correct boresight angles. This cloud is shown again in Figure 3.34 overlayed onto an image of the beach where Maverick took the data.

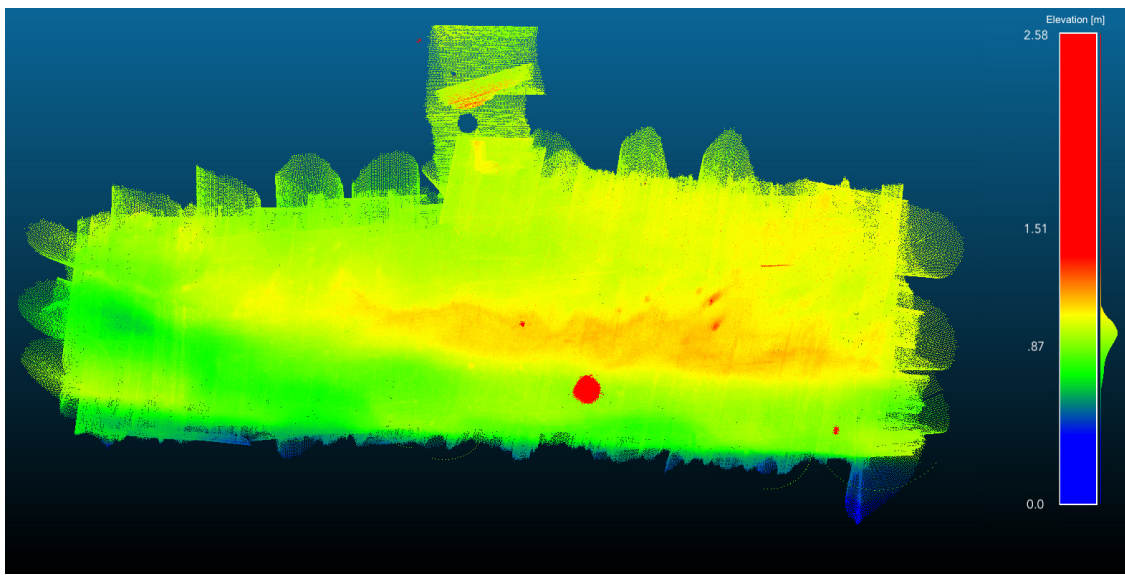


Figure 3.32: Final fully boresighted point cloud.

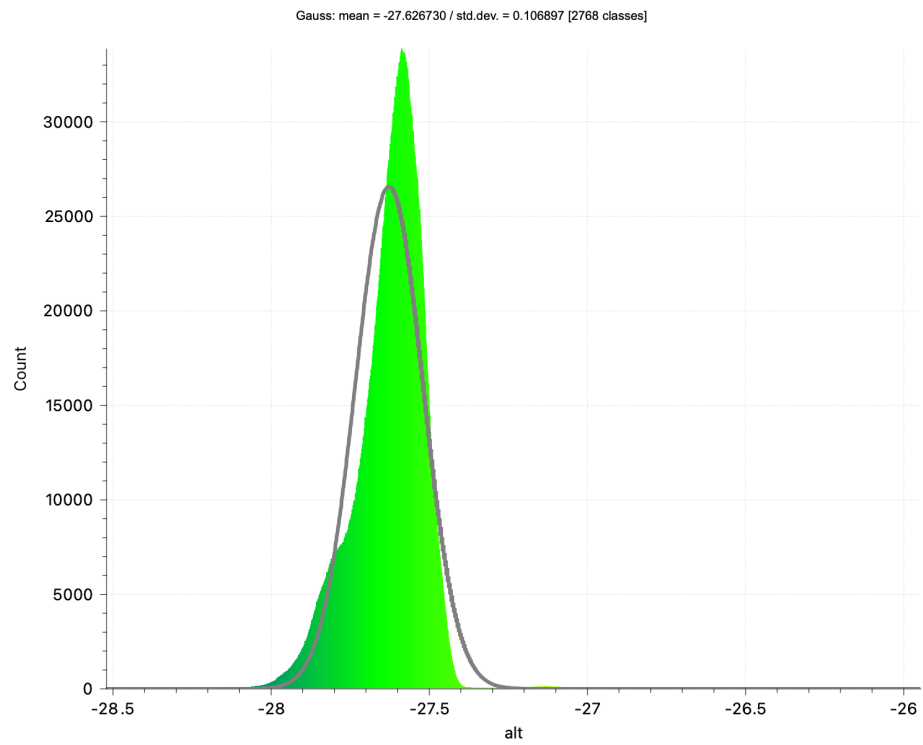


Figure 3.33: Gaussian distribution of elevation values for the final cloud with all corrections applied displayed in Figure 3.32.

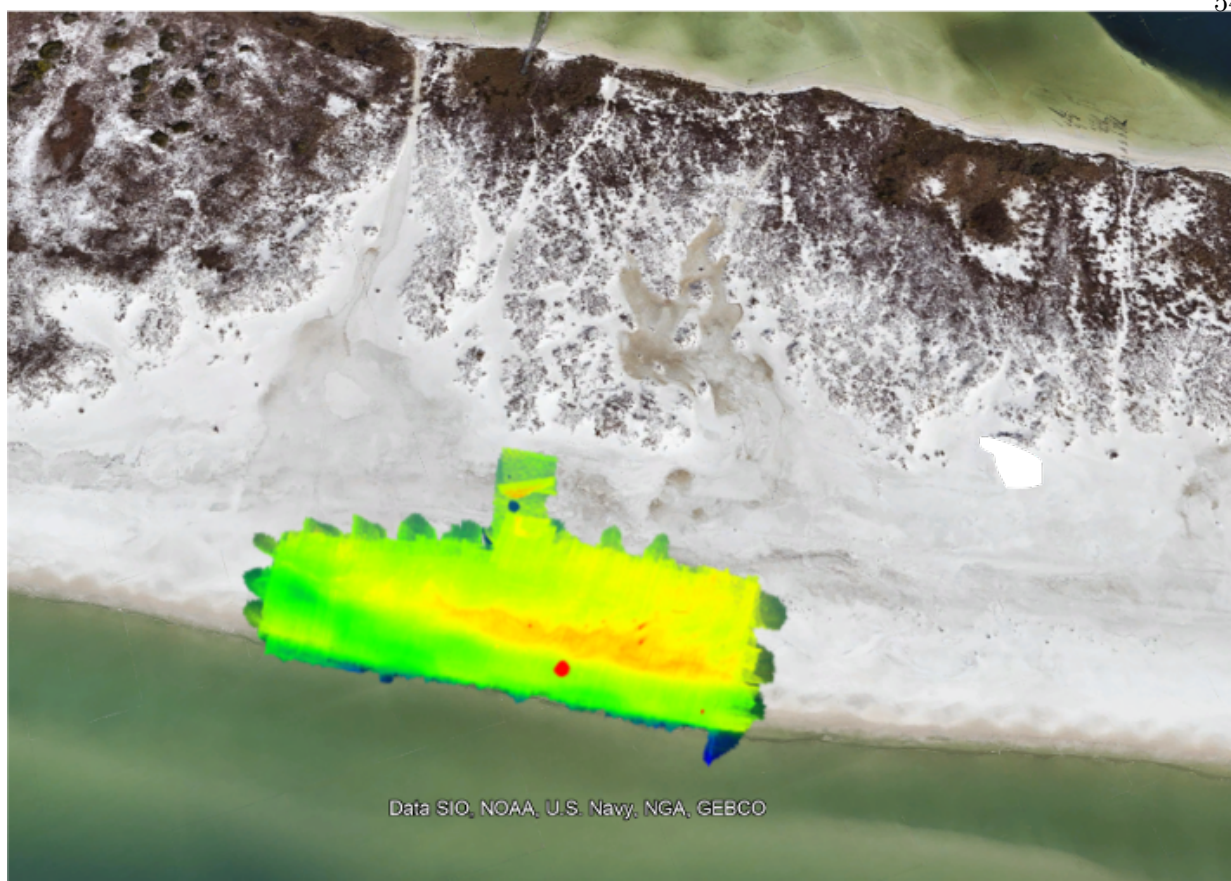


Figure 3.34: Final fully boresighted point cloud overlayed onto the beach.

Chapter 4

Conclusions

Given the findings in Chapters 2 and 3, it is useful to revisit and discuss the initial assumptions. Each assumption is reconsidered given the findings reported throughout this thesis through which its validity is determined. The goal was to analyze these assumptions in order to improve pointing knowledge and pointing accuracy. To achieve the desired horizontal resolution of 5cm from a distance of 30m, a pointing accuracy of $\pm 0.1^\circ$ was required.

4.1 Assumption A1

Assumption A1 is that every scan contains evenly distributed pointing angles. First, in Section 3.2, unevenness in the scan was discovered due to the slight translation of the x position of the beam from the PM rotation, creating an asymmetric light cone. This translation, however, is determined to be negligible as it is on the order of 1mm.

Another source of unevenness was discovered in Section 3.3.5 from the varying time ratios that were expected to be stable. This instability limits the capabilities to relate pointing angle to time, which is currently the basis of angle assignment (see Eq 1.8). However, given that each scan is three times as long as a swath, it is still unknown how good (or bad) this assumption is within each swath. More information is required to quantify the swath-specific unevenness. Section 5 contains some suggestions for how to acquire this extra information.

The source of this ratio's 0.1 variance as calculated by Eq 3.2 has two main components: the instability of the mirror rotation rate, both innate and from UAV motion, and the incomplete return

swaths. Incomplete swaths are why averaging was required in the first place, so their presence will certainly appear as a variance in the data. However, the dataset taken during the least-time test, where the unit was unmoving and expected full returns, underwent the same ratio testing, and there was still a standard deviation of .02, resulting in a smaller, but still significant angle uncertainty of $\pm.2^\circ$. This is much less than the standard deviation of the typical flight data sets, however, the fact that it's still not 0 suggests there is some inherent instability in the mirror motion. This conclusion is unfortunate, especially considering one of the metrics that make PMs ideal for LiDAR is their steady velocity. However, it is essential to recognize this unsteady motion for maximum possible pointing knowledge. Overall, assumption A1 is false, but is, with current capabilities, still required for processing.

4.2 Assumption A2

Assumption A2 is that the pointing angle in the middle of the aperture is at 0° . Initial system modeling almost immediately disproved the A2 assumption. Subsequently, all modes of testing continued to disprove this assumption. While, as previously discussed, boresighting could correct this offset, it was a misguided correction. Additionally, the least-time test designed to determine this central offset angle can be replicated with any PM scanning LiDAR system with processes similar to Maverick's. Given its success, the standardization of this test is recommended for all future Maverick units built.

The direct improvement on the pre-boresighted point cloud provided by the offset angle, $\theta_{off} \approx 1.7^\circ$, and the substantial reduction of the necessary roll direction boresighting angle suggests that this test did very accurately discover the offset for the unit collecting the presented data. The slight difference between this value, the offset found in the model, and the offset found by the wall measurement test suggests that while the model provides a good baseline for all unit offset values, an empirical test is needed on a unit-by-unit basis. The discovery of this offset added quite a bit to the collection of pointing knowledge of the Maverick system, as was the primary goal of this research.

4.3 Assumption A3

The A3 assumption that 30° of light exits the aperture was another immediately disproven. The model and test both did agree on the actual value of 30.5° suggesting it accurately describes the system. Within data processing, this will only make a small change in deciding what angles are considered acceptable returns rather than noise from inside the box. This value is problematic, however, given the limited receiver capabilities. Section 3 briefly mentions this point, but it is discussed further in Section 5.

Despite the 30.5° exit swath, the received swath will only sometimes span the whole FOV, a common source of difficulty within the processing. First off, it makes the middle of each swath challenging to find. If one side of returns cuts off, or there is a gap in the middle, it can become an almost impossible problem to resolve within the code. That is why taking average ratios throughout the swath becomes necessary to resolve those uncertain areas. However, returning to the previous conclusion, if the ratio of time it takes for the beam to travel between the D1 and D2 detectors and back is inconsistent, then this averaging compounds errors. Of course, a slight standard deviation is expected and stems from the incomplete swaths, but the magnitude of this error suggests physical sources, too.

4.4 Overall Conclusions

Unfortunately, despite all the different tests and error metrics, it is still difficult to give an exact value to Maverick's pointing accuracy. However, the quantifiable uncertainty is at least $\pm 1^\circ$ due to the instability in the mirror motion while in flight. This exceeds the desired $\pm 0.1^\circ$ to achieve positioning at 5cm from a 30m distance, instead resulting in a horizontal accuracy of $\pm 58\text{cm}$. Even the much more controlled static LiDAR test resulted in an uncertainty of $\pm 2^\circ$, exceeding the requirement and created a horizontal uncertainty of $\pm 12\text{cm}$.

Some positive takeaways include the definition of the central angle offset and the overall repeatability of the wall scan test. Additionally, the identification of the D1 angle and validation of its

value through ratio analyses. The output swath size has been better defined compared to previous iterations. On the processing side, incorporating these correct angle values has sharpened the range of z elevations. Furthermore, algorithmic enhancements have led to more defined representations of objects and clearer landscapes in the horizontal direction.

The primary sources of error that will lead to uncertain pointing angles are the innate unsteady velocity of the PM and the additional perturbations that seem to occur from flight. These sources of uncertainty will inherently worsen an algorithm that associates a pointing angle with a time interval. However, with only the pointing information from one D1 detector, it is very difficult to get around this limitation. The inconsistency in the returns is also directly coupled with this issue. When employing averaging to find the center of each swath, if the PM velocity through any specific swath is different from the mean, the algorithm will place the center of that swath incorrectly. Given the small magnitude of this instability and due to positive visual validation of the results, the impact of these instabilities doesn't seem overly aggressive. Supplementary work, as described in Section 5, is needed to quantify these effects fully and advance pointing accuracy as much as possible.

As mentioned in Section 1, there are many possible errors in this LiDAR data beyond those associated with pointing. Upon inspection of the final point clouds, we still see some minor errors, but their exact origin, whether it is pointing related or not, could not be identified within the scope of this thesis. Through all the points outlined in this conclusion, the pointing knowledge of the PM system within Maverick has certainly improved, other opportunities for future improvements to the system identified.

Chapter 5

Further Work

Many of the uncertainties discussed throughout this thesis boil down to the variability in the mirror rotational velocity. If this velocity remained perfectly consistent throughout data collection, assigning pointing angles would be much easier, as all instances of a pointing angle would occur at dependable intervals. All processing solutions discussed in Section 3 rely on only two distinct types of data points per swath to fully describe the system's pointing – the center of the D1 detections and the average center of the D2 detections. The interpretation of this information suggests that throughout a whole scan, the velocity is steady, which has proven untrue. If another detector is added at the other end of the swath after the beam completes its pass through the aperture, this information could assist in understanding the velocity throughout a single swath. Generally, the steadiness of the mirror for the rest of the scan when the beam is not exiting the aperture is irrelevant. This extra reference information could help better understand the mirror's behavior in a smaller, more vital area.

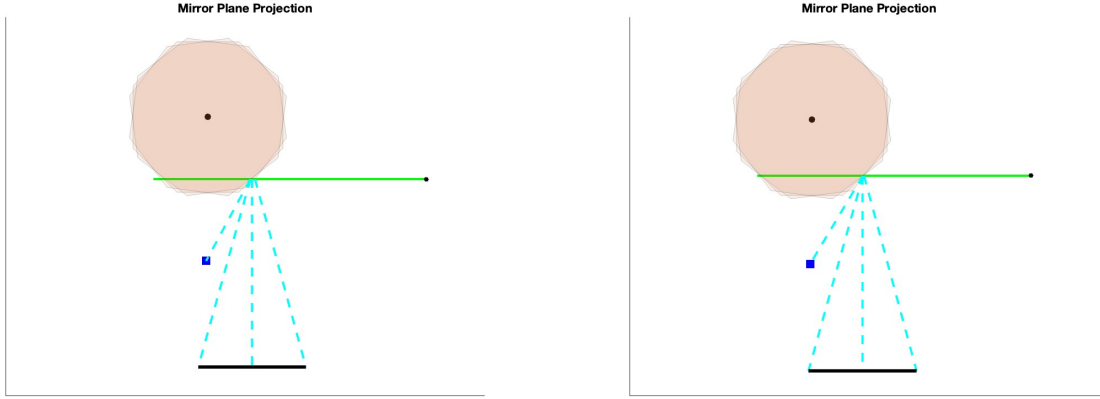
With increased pointing knowledge, there is also an opportunity to improve Maverick's pointing capabilities. General improvements can also help accuracy tangentially by providing better LiDAR returns to reference and lowering the noise that currently leads to processing issues. There are three pertinent solutions to this – change the aperture, move the laser, or increase the number of sides of the polygon.

Changing the aperture to improve pointing can also take multiple forms; the first option is increasing the aperture size to widen the system's scan plane. A generic system whose scan range

is -15° to 15° and flies 30 m above the ground sees a horizontal swath of 15 meters. If the angular range increases to -20° to 20° , the horizontal swath for the same height increases to 22 meters. However, the main benefit of this change is simply allowing extra light to exit the LiDAR system rather than contributing to internal noise. The receivers would also need to be updated to detect this larger FOV. With the larger aperture and increased FOV receivers, the system could likely measure more bathymetry and topography. However, due to the specular reflections of light off the water surface, those returns would not see any benefit.

Another, simpler, suggestion is to move the aperture over. Section 3 first mentions that the receivers have limited FOV capabilities, as demonstrated by the curved tail in Figure 3.16. Physically moving the aperture over on the x axis would recenter those angles so the receivers could accurately read the outer angles. Specifically, the receivers are optimized for a FOV of $\pm 15^\circ$. Despite this, when $\theta_{off} = 1.7^\circ$, the highest positive angles reach approximately 16.7° . The receivers will not inherently miss these every swath but do struggle with those higher angles. This modification would also reinstate the initial a2 assumption that 0° is in the center of the aperture. Figure 5.1a shows the model of this scenario using the same program as used in Section 3. Changing the location of the aperture and subsequent exiting angles will inherently change the asymmetric geometry of the system. In this scenario, however, the offset will still negligibly be $< 1mm$.

This same centering effect could be achieved by adjusting the value of Maverick's z_{laser} . As Section 3.2 discovered, there does seem to be a significant effect of the relationship of the z_{laser} and polygon sidelength a variables for symmetric beam behavior. Using this information, by adjusting the position of the laser in Maverick by only 0.2cm, the same effect as moving the aperture is achieved. As shown in Figure 5.1b, the central angle loses the θ_{off} and is now just 0° .



(a) Simulation moving the aperture along the x axis.

(b) Simulation adjusting the z_{laser} .Figure 5.1: Simulated changes resulting in a 0° central angle.

One way to increase the percentage of the scan exiting the system without changing the aperture is to increase the number of facets of the scan mirror. As described in Eq 2.1, doubling the number of facets would half the size of the scan. Specifically, a 16-facet mirror would mean $\alpha = 22.5^\circ$ and produce a full swath width of 45° . The correct mirror placement within the system ensures it still directs the light into the aperture. Given this proper placement, nothing else about the system would need to change. This change would increase point density, decrease noise, and generally better use the power the system is already drawing.

In summary, this study emphasizes the importance of scanning error reduction for ALB systems. Through rigorous analysis and testing, notable enhancements in data alignment and object size accuracy were achieved. Proposed mechanical solutions hold promise for further refining LiDAR pointing capabilities for small object detection within bathymetric mapping.

Bibliography

- [1] Fermat's principle and the laws of reflection and refraction. Pearson, 2009.
- [2] Yves Pastol Elisa Casella Alessio Rovere Lauric Thiault Benoît Espiau Gilles Siu Franck Lerouvreur Nao Nakamura James L. Hench Russell J. Schmitt Sally J. Holbrook Matthias Troyer Antoine Collin, Camille Ramambason and Neil Davies. Very high resolution mapping of coral reef state using airborne bathymetric lidar surface-intensity and drone imagery. International Journal of Remote Sensing, 39(17):5676–5688, 2018.
- [3] CloudCompare. Gpl software. Retrieved from <http://www.cloudcompare.org/>.
- [4] PhD David S. Loshin, OD. The Geometrical Optics Workbook. Butterworth-Heinemann, Newton, MA, 1991.
- [5] Virgil-Florin Duma and Maria-Alexandra Duma. Optomechanical analysis and design of polygon mirror-based laser scanners. Applied Sciences, 12(11), 2022.
- [6] Xiaolu Li et al. Airborne lidar: state-of-the-art of system design, technology and application. Measurement Science and Technology, 32, 2020.
- [7] Gentec-EO. The laser wavelength chart explained. <https://www.gentec-eo.com/blog/the-laser-wavelength-chart-explained>.
- [8] Dennis H. Goldstein. Polarized Light. Taylor Francis Group, Boca Raton, FL, 2011.
- [9] Hamamatsu. Compact, high performance electromagnetically driven mems mirror for two-dimensional laser scanning s13989-01h. https://www.hamamatsu.com/jp/en/news/featured-products_and_technologies/2019/20191106000000.html.
- [10] Shimadzu Scientific Instrument. Relative diffuse reflectance measurement. www.ssi.shimadzu.com/products/uv-vis/uv-vis-nir-spectroscopy-consumables/relative-diffuse-reflectance-measurement/index.html.
- [11] J.L. Irish and T.E. White. Coastal engineering applications of high-resolution lidar bathymetry. Coastal Engineering, 35(1):47–71, 1998.
- [12] Lokesh J. Mem: The tiny technology with big impacts. <https://www.linkedin.com/pulse/mems-tiny-technology-big-impacts-lokesh-j/>, 2023.
- [13] Joni. Welford's method for computing variance. <https://jonisalonen.com/2013/deriving-welfords-method-for-computing-variance/>, 2013.

- [14] Zhuoxiao Li, Zitian Peng, Zheng Zhang, Yijie Chu, Chenhang Xu, Shanliang Yao, Ángel F. García-Fernández, Xiaohui Zhu, Yong Yue, Andrew Levers, Jie Zhang, and Jieming Ma. Exploring modern bathymetry: A comprehensive review of data acquisition devices, model accuracy, and interpolation techniques for enhanced underwater mapping. In Frontiers in Marine Science, 2023.
- [15] LiteWave. University of hawaii point cloud. Private Communication, 2022.
- [16] Yue Ma, Nan Xu, Jinyan Sun, Xiao Hua Wang, Fanlin Yang, and Song Li. Estimating water levels and volumes of lakes dated back to the 1980s using landsat imagery and photon-counting lidar datasets. Remote Sensing of Environment, 232:111287, 2019.
- [17] Gerald F. Marshall and Glenn E. Stutz. Handbook of Optical adn Laser Scanning. CRC Press, Rochester, NY, 2012.
- [18] Scanner MAX. Saturn-1 galvo. <https://scannermax.com/collections/single-axis-galvos/products/saturn-1-galvo>, 2023.
- [19] National Ocean and Atmoshpéric Science. What is sonar? <https://oceanservice.noaa.gov/facts/sonar.html>, 01/20/23.
- [20] Roger Hinrichs Paul Peter Urone. College physics 2e. <https://openstax.org/books/college-physics-2e/pages/25-3-the-law-of-refraction>, 2022.
- [21] Thinal Raj, Fazida Hanim Hashim, Aqilah Baseri Huddin, Mohd Faisal Ibrahim, and Aini Hussain. A survey on lidar scanning mechanisms. Electronics, 9(5), 2020.
- [22] SBG Systems. Quanta series. <https://www.sbg-systems.com/products/quanta-series/>, 2018.
- [23] Precision Laser Scanning. Mems mirrors vs polygon scanners for lidar in autonomous vehicles. <https://precisionlaserscanning.com/2017/12/mems-mirrors-vs-polygon-scanners-for-lidar-in-autonomous-vehicles/>, 2017. georgehelser.
- [24] Matthew Strathman, Yunbo Liu, Ethan G. Keeler, Mingli Song, Utku Baran, Jiefeng Xi, Ming-Ting Sun, Ruikang Wang, Xingde Li, and Lih Y. Lin. Memscanning micromirror for optical coherence tomography. Biomed. Opt. Express, 6(1):211–224, Jan 2015.
- [25] Dingkang Wang, Connor Watkins, and Huikai Xie. Memscanning mirrors for lidar: A review. Micromachines, 11(5), 2020.